ADVANCED MATERIALS
www.advmat.de

Chiral Metal Halides toward Circularly Polarized Photodetectors

Yarong Gu, Xinyu Zhang, Ziqing Li, and Xiaosheng Fang**

Circularly polarized (CP) photodetection has become a cornerstone technology in advancing fields such as quantum communication, biomedical imaging, and secure optical encryption. Conventional CP photodetectors relying on external optical components face challenges in miniaturization and efficiency, driving the exploration of chiral-sensitive materials for direct polarization discrimination. Among these, chiral metal halides have emerged as a revolutionary platform due to their intrinsic spin-orbit coupling, structurally tailorable chirality, and solution processability, enabling unprecedented photocurrent dissymmetry factors and broad absorption wavelengths. This review comprehensively examines the fundamental principles, material innovations, and device engineering strategies underpinning chiral metal halide-based CP photodetectors. Furthermore, representative applications of chiral metal halide-based CP photodetectors exploiting their emergent properties in high-precision circular polarization imaging, dynamic information encryption and bionic neuromorphic perception are examined. Finally, persisting challenges and future research directions are outlined for chiral metal halide-based CP photodetectors.

1. Introduction

Circularly polarized (CP) light photons carry spin angular momentum, enhancing spatial distribution characteristics beyond conventional photodetector parameters such as light intensity and wavelength. CP light detection expands information encoding capabilities with additional parameters like orbital angular momentum (OAM), polarization degree, azimuth angle, ellipticity, and optical rotation direction.[1,2] This multidimensional capability enhances information transmission and discrimination, offering unique advantages in advanced applications such as quantum communication, biomolecular chiral recognition, and 3D display technologies.[2–5] However, traditional CP light detection systems relying on cascaded quarter-wave plates and linear polarizers suffer from increased bulk, complexity, and cost, limiting their practical applications.

Recent years have witnessed significant research interest in CP photodetectors based on chiral materials or chiral structures (**Table 1**), owing to their intrinsic capacity for direct CP light signal discrimination. Chiral organic material systems, particularly spiroene derivatives, exhibit primary absorption in the ultraviolet (UV) region.[6–8] While blending with materials like anthracene derivatives can extend absorption into the visible range and enhance the absorption dissymmetry factor (g_{abs}), these systems typically suffer from low photocurrent generation.[9–12] Covalent organic frameworks demonstrate notable responsivity ≈450 nm, yet their detectivity remains limited (≈10^8 Jones).[13,14] In contrast, non-fullerene acceptor blends achieve higher detectivity (≈10^{13} Jones).[15] Structurally chiral metamaterials offer distinct advantages for long-wavelength CP light detection, typically beyond 1000 nm.[16–18] However, their optical response critically depends on precise geometric parameter design, constraining device bandwidth and process compatibility. Against this backdrop, chiral metal halides distinguish themselves through their broad spectral responsivity spanning UV to near-infrared (NIR) wavelengths,[19–32] exceptionally high photocurrent anisotropy factors (g_{Iph}) approaching the theoretical limit ($|g_{Iph}| = 2$),[33,34] and unique properties—including significant Rashba splitting,[35,36] intrinsically strong spin-orbit coupling,[37,38] and prolonged spin lifetimes.[37,39] Furthermore, the inherent scalability of chiral metal halides facilitates their coupling with functional materials (e.g., carbon nanotubes,[29] liquid crystals[34]), enhancing overall device performance metrics such as responsivity. These collective advantages position chiral metal halides as highly competitive candidates for direct CP light detection.

Chiral metal halides—represented most prominently by hybrid organic-inorganic metal halides (HMHs)—have consequently become a frontier research focus for direct CP light detection due to the synergistic effects of chiral properties and

Y. Gu, X. Zhang, X. Fang
College of Smart Materials and Future Energy
State Key Laboratory of Molecular Engineering of Polymers
Shanghai 200433, P. R. China
E-mail: xshfang@fudan.edu.cn
Z. Li
State Key Laboratory of Photovoltaic Science and Technology
Shanghai Frontiers Science Research Base of Intelligent Optoelectronics and Perception
College of Future Information, Institute of Optoelectronics
Fudan University
Shanghai 200433, P. R. China
E-mail: lzq@fudan.edu.cn

The ORCID identification number(s) for the author(s) of this article can be found under https://doi.org/10.1002/adma.202508016

DOI: 10.1002/adma.202508016

Table 1. Figures of merit for different types of CP photodetectors.

Category	Materials	Wavelength [nm][a]	$\|g_{abs}\|$[b]	$\|g_{Iph}\|/\|g_{res}\|$[c]	Responsivity [A W^{-1}]	Detectivity [Jones]	Refs.
Organic materials	Chiral 1-aza[6]helicene	365	≈0.001	1.8	\	\	[7]
	Chiral organic semiconductors	385	≈0.001	≈0.05	314	3.9×10^{12}	[8]
	Chiral multiple helicene/ 2,6-diphenylanthracen	556	0.0016	0.24	0.28	\	[10]
	Chiral squaraine/$PC_{61}BM$	543	≈0.09	0.1	\	\	[11]
	Chiral diketopyrrolopyrrole-hexathiophene/$PC_{61}BM$	606	0.02	0.17	0.28	1.8×10^{10}	[12]
	Chiral covalent-organic frameworks	405	0.00045	≈0.5	1.05	5.25×10^{8}	[13]
	Chiral covalent-organic frameworks	450	\	0.276	4.423	5.25×10^{8}	[14]
	Non-fullerene acceptor blends	700	≈0.0001	0.113	\	1.04×10^{13}	[15]
Metal halides	Chiral 1D lead halide	395	0.02	0.1	0.797	7.1×10^{11}	[20]
	Chiral 1D lead halide	395	0.04	1.85	0.28	\	[33]
	Chiral 1D lead halide	398	0.042	0.7	0.96	5.23×10^{13}	[21]
	Chiral quasi-2D lead halide	532	\	0.2	1.1	2.3×10^{11}	[22]
	Chiral quasi-2D lead halide	800	\	0.03	8.1×10^{-5}	1.2×10^{9}	[23]
	Chiral 2D lead halide	495	0.00117	0.65	1.06	\	[24]
	Chiral 2D lead halide	800	\	0.1	3.5×10^{-6}	\	[25]
	Chiral 3D lead halide	320	0.000076	0.28	\	\	[26]
	Chiral bimetal halide	500	0.0016	0.44	0.14	1.63×10^{11}	[27]
	Chiral Rashba Ferroelectrics	430	\	0.2	0.0419	2.4×10^{12}	[28]
	Chiral copper chloride-carbon nanotube	405	0.05	0.25	452	\	[29]
	Chiral 2D lead halide/3D lead halide	520	\	0.67	0.0012	1.1×10^{12}	[30]
	Chiral 2D lead halide/Chiral quasi-2D lead halide	510	\	0.38	22.14	\	[31]
	Chiral 2D lead halide-TADDOL	491	0.00579	1.16	0.17	3.63×10^{12}	[32]
	Lead halide-liquid crystals	532	1.7	1.96	0.294	\	[34]
Chiral metamaterials	Chiral plasmonic nanoparticles	780	≈0.062	0.57	6.5	2×10^{10}	[16]
	Chiral plasmonic metamaterials	1340	0.72	1.03	0.0022	\	[17]
	Chiral plasmonic metamaterials	2200	1.24	1.56	33900	1.8×10^{11}	[18]

[a] Wavelength refers to the detection wavelength of the CP photodetector; [b] Some $|g_{abs}|$ at specific detection wavelengths are either obtained directly from reference data using professional software or calculated using Equation (3); these may differ from reported maxima or peak-absorption $|g_{abs}|$; [c] Some $|g_{Iph}|/|g_{res}|$ are calculated using either Equations (8) or (9), based on reference data.

semiconductor photoelectric properties.[1,19,40–43] By integrating chiral organic molecules with metal halide frameworks, these materials retain metal halide advantages (e.g., high carrier mobility, broadband absorption, strong photoluminescence) while exhibiting intrinsic chirality through circular dichroism (CD), circular polarized photoluminescence, spin, and second-harmonic generation.[19,44] In addition, their structural tunability provides a broad space for performance optimization. Adjusting the halogen composition (e.g., the Br/I ratio), metal center (e.g., Pb/Sn), or chiral ligands enables precise modulation of bandgap, exciton binding energy, and chiral response wavelengths across ultraviolet-visible (UV–vis) to NIR ranges. Such versatility supports applications in flexible photodetectors, quantum encryption, and biochiral sensing, paving the way for miniaturized, low-power integrated CP detection systems.

Figure 1 outlines the evolution of chiral metal halides toward CP photodetectors. The field began with the synthesis of 1D chiral lead halides using $(S\text{-}C_6H_5C_2H_4NH_3)^+$ cations in 2003,[45] followed by 2D chiral lead halides in 2006.[46] Early studies focused on synthesis until 2017, when their CD properties were characterized.[47] Subsequent advances in 2019 yielded the chiral metal halides-based CP photodetector,[48] spurring rapid progress in device performance metrics such as wafer-scale fabrication, near-theoretical anisotropic photocurrents, and polarization-state resolution.

Below, this review systematically examines chiral metal halides toward CP photodetection. First, the principles and key performance metrics of CP photodetectors are summarized. Then, by classifying the structural levels in the intra-crystal, interface and beyond-crystal levels in metal halides, chiral regulation strategies and chiral generation mechanisms at different levels are discussed. Subsequently, the research progress and emerging applications of CP light detection devices based on chiral metal halides are outlined. Finally, perspectives on the challenges and future development in this field are presented.

2. Fundamentals of Circularly Polarized (CP) Photodetectors

The detection of CP light typically relies on light-matter interactions, particularly in chiral systems or materials exhibiting spin-orbit coupling. Owing to their strong intrinsic spin-orbit

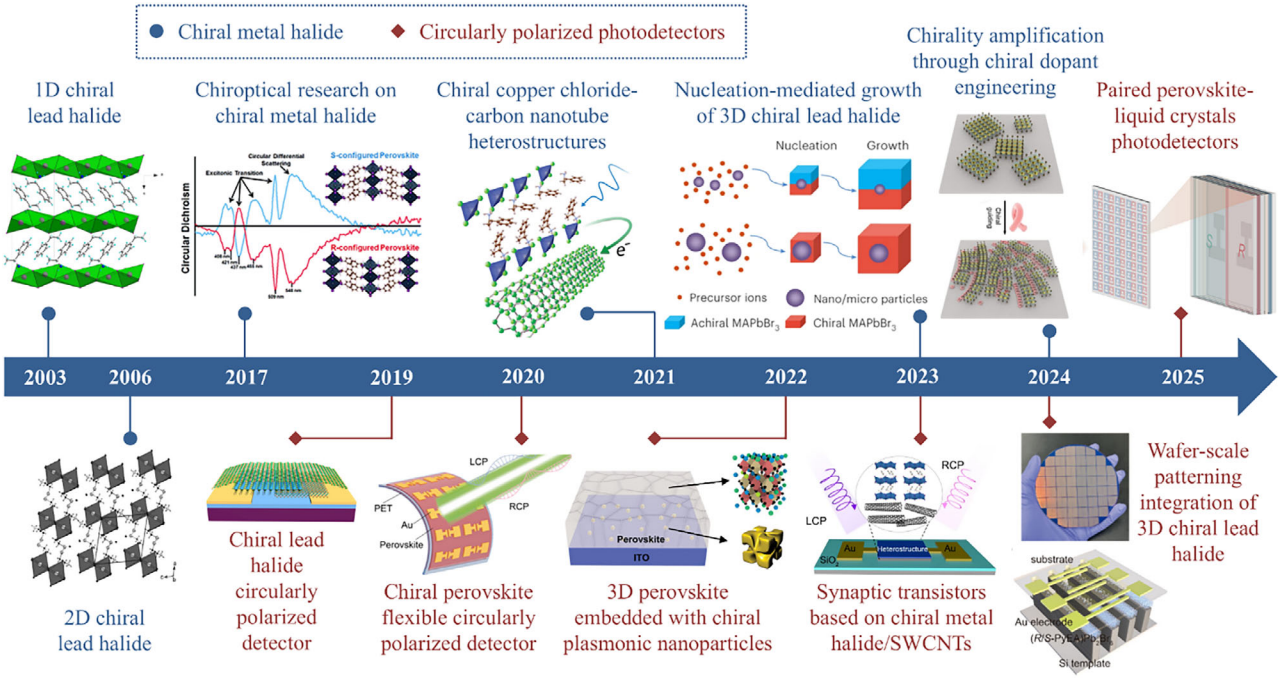

Figure 1. Timeline of research on chiral metal halides toward CP photodetectors. Timeline showing key events in the development of chiral metal halides toward CP photodetectors. Reproduced with permission.[45] Copyright 2003, International Union of Crystallography. Reproduced with permission.[46,47] Copyright 2006, 2017, The Royal Society of Chemistry. Reproduced with permission.[29,48,49] Copyright 2021, 2019, 2024, American Chemical Society. Reproduced with permission.[22,50] Copyright 2020, 2022, Wiley-VCH. Reproduced with permission.[51,52] Copyright 2023, Springer Nature. Reproduced with permission.[32] Copyright 2024, American Association for the Advancement of Science. Reproduced with permission.[34] Copyright 2024, Elsevier.

coupling and inherently chiral lattice symmetry, chiral metal halides simultaneously possess circular dichroism and chiral-induced spin selectivity, thereby providing an efficient platform for polarization-sensitive photodetection.

2.1. Effects and Theories Associated with CP Photodetectors

2.1.1. Circular Dichroism (CD)

CD arises from the differential interaction of chiral materials with left- and right-handed circularly polarized (LCP/RCP) light, manifested as distinct absorption coefficients for the two polarization states. This intrinsic chiroptical phenomenon originates from the asymmetric electronic transitions in chiral systems, where molecular or crystalline handedness dictates preferential absorption of specific circular polarizations (**Figure 2**a,b). CD spectroscopy serves as the principal experimental method to quantify this effect. The technique records ellipticity (θ, mdeg), a parameter directly proportional to the absorption difference through:[19]

$$\theta\ (\text{mdeg}) = \Delta A \left(\frac{\ln 10}{4}\right)\left(\frac{180000}{\pi}\right) \quad (1)$$

where ΔA is the difference in absorption between LCP and RCP light (A_L and A_R). When the CD of chiral materials is weak (i.e., $\Delta A \ll 1$), the calculation formula for θ can be simplified to:[53]

$$\theta\ (\text{mdeg}) = 32980 \times \Delta A \quad (2)$$

To account for sample-dependent variables including crystalline orientation and thickness, the absorption dissymmetry factor (g_{abs}, which is also expressed by g_{CD} in some literatures) serves as a normalized metric for CD intensity comparison:[1,3,19]

$$g_{abs} = 2 \times \frac{A_L - A_R}{A_L + A_R} = \frac{\theta}{32980 \times \Delta A} \quad (3)$$

where A_L and A_R are the absorbance of LCP and RCP lights. When $g_{abs} = 0$, the material is achiral (exhibiting no chiral characteristics); at $g_{abs} = \pm 2$, complete absorption of either LCP or RCP light is achieved.

Beyond linear absorption, chiral metal halides also exhibit the second harmonic generation circular dichroism (SHG-CD) effect, where CP light of opposite handedness induces varying second harmonic generation (SHG) efficiencies due to the materials' asymmetric centers and intrinsic chirality.[54–56] The circular polarization sensitivity of SHG is evaluated by the anisotropic factor ($g_{SHG\text{-}CD}$), calculated from differential SHG intensities under LCP and RCP illumination (I^L_{SHG} and I^R_{SHG} *I*R):[57]

$$g_{SHG-CD} = 2 \times \frac{I^L_{SHG} - I^R_{SHG}}{I^L_{SHG} + I^R_{SHG}} \quad (4)$$

Their non-centrosymmetry makes them promising for nonlinear chiroptical applications and chiral photonic circuits.[19,58–60] SHG-CD in low-dimensional systems enables NIR CP light

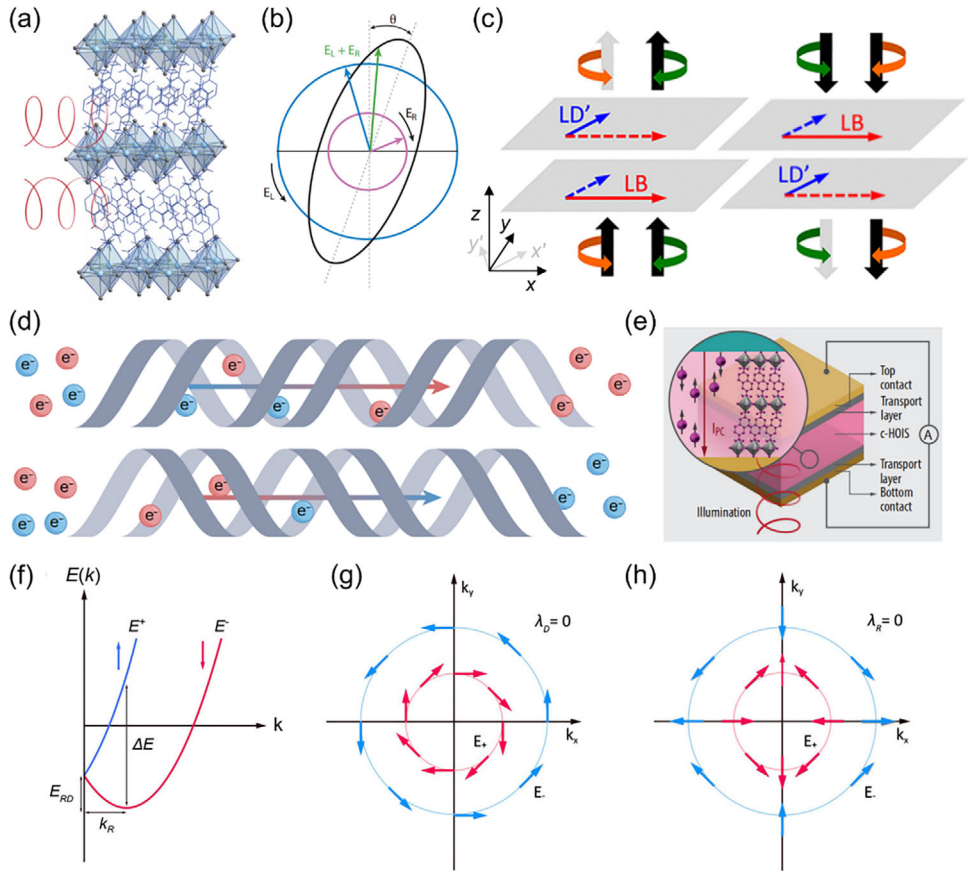

Figure 2. Effects and theories associated with CP photodetectors: a,b) Differential absorption of the left (E_L)- and right (E_R)-hand polarized light induces ellipticity (θ). Reproduced with permission.[38] Copyright 2025, Annual Reviews. The resulting amplitude imbalance causes the beam to recombine into elliptically polarized light. c) LD/LB interactions (part of) for transition dipoles in light propagation direction (z), where solid/dashed arrows denote contributions to dichroism (LD′) or birefringence (LB). Reproduced with permission.[63] Copyright 2021, American Chemical Society. d) CISS effect-driven electron spin filtering in chiral materials. Reproduced with permission.[2] Copyright 2025, Springer Nature. e) CP photodetectors architecture using c-HOIS (chiral hybrid organic-inorganic perovskite semiconductors). Reproduced with permission.[38] Copyright 2025, Annual Reviews. f) Energy difference (ΔE) and momentum splitting (k_R) between inner (E_+, in red) and outer (E_-, in blue) sub-bands.[84] Spin textures for g) pure Rashba ($\lambda_D = 0$) and h) pure Dresselhaus ($\lambda_R = 0$) spin-splitting, originating from site and bulk inversion asymmetry, respectively. Reproduced with permission.[84] Copyright 2024, American Chemical Society.

discrimination, overcoming the bandgap limitations of conventional UV-vis detection.

Notably, solid-state CD measurements of chiral metal halides face inherent challenges from macroscopic anisotropy-induced artifacts. Mueller matrix analysis reveals that genuine CD ($CD_{genuine}$) from intrinsic chirality must be decoupled from linear dichroism (LD) and birefringence (LB) effects (Figure 2c) through:[61–64]

$$\mathrm{CD} \approx CD_{\mathrm{genuine}} + 0.5\left(\mathrm{LD}' \cdot \mathrm{LB} - \mathrm{LB}' \cdot \mathrm{LD}\right) + (-\mathrm{LD}) \cdot \sin\alpha \cdot \cos 2\theta \quad (5)$$

where LD/LD' and LB/LB' denote linear dichroism and birefringence components in the x-y plane (perpendicular to optical axis z) and along its bisectors (+45° offset), respectively, the azimuth angle θ specifies the sample's rotational orientation around the incident light axis, and α quantifies the residual birefringence inherent to the spectrometer's photoelastic modulator. The LD and LB contribution exhibits sign reversal upon film inversion, enabling quantification of $CD_{genuine}$ and LDLB effects through comparative measurements:[61,62,65]

$$CD_{\mathrm{genuine}} = 0.5\left(CD_{\mathrm{front}} + CD_{\mathrm{back}}\right) \quad (6)$$

$$\mathrm{LDLB} = 0.5\left(CD_{\mathrm{front}} - CD_{\mathrm{back}}\right) \quad (7)$$

The dimensionality dependence of CD signals reveals distinct mechanistic origins. 0D and 1D chiral metal halides films demonstrate composite CD signals from molecular-level chirality and mesoscopic anisotropic domains, whereas in 2D chiral metal halides films, the LDLB effect is negligible.[61] Particularly in certain HMH derivative films, film morphology introduces additional complexity in CD interpretation beyond conventional LD and LB contribution, highlighting the necessity for advanced structural characterization.[62]

2.1.2. Chiral-Induced Spin Selectivity (CISS) Effect

The CISS effect refers to the phenomenon in which chiral materials selectively filter the electron spin direction through their asymmetric structure—a key mechanism for spin-polarized charge transport in chiral metal halides.[39,44,66,67] Although substantial theoretical progress has been made, a comprehensive quantitative framework remains elusive, and the microscopic origin is still debated.[2,68,69] A prevailing hypothesis suggests that the helical structure or asymmetric electric field of chiral molecules induces an effective magnetic field perpendicular to the electron's transport direction, resulting in energy splitting between the two degenerate spin states.[44,68,70,71] As illustrated in Figure 2d, this results in one spin (e.g., up, red) encountering a lower transmission barrier than the other (down, blue), enabling chirality-dependent spin filtering.[2,67,72,73]

In CP photodetectors, spin-polarized carriers generated by CP light exhibit chirality-dependent transport behavior governed by the CISS effect within the chiral material layer (Figure 2e).[38,72] This process requires neither external magnetic fields nor ferromagnetic materials. However, the contribution of CISS in different device architectures remains controversial.[70] In photodiodes with out-of-plane carrier transport, the conventional CISS model is generally applicable. By contrast, for in-plane transport configurations—such as photoconductors and phototransistors—the underlying mechanism remains contentious: some studies propose that Rashba splitting dominates,[74] whereas others argue that CISS contributes via interfacial spin filtering, as evidenced in chiral metal halide/carbon nanotube systems.[29,75,76] Although direct quantification of CISS remains challenging, its effects can be indirectly evaluated using conventional performance parameters such as the anisotropy factor of responsivity.[38]

2.1.3. Spin-Orbit Coupling (SOC)

The CISS effect arises from the spin-selective electron transport through chiral materials, and its theoretical foundation can be traced to SOC.[77,78] Metal halides exhibit strong intrinsic SOC effects primarily due to the high atomic nuclear charge of heavy metal elements (e.g., Pb and Bi), leading to robust coupling between electron spin and orbital angular momentum during their motion.[79–81] In the absence of time-reversal or spatial inversion symmetry, SOC lifts the spin degeneracy in momentum space, splitting the degenerate spin up ($\varepsilon_k^{\uparrow}$) and spin down ($\varepsilon_k^{\downarrow}$) states.[82,83] This spin splitting manifests as a shift in energy bands along the reciprocal space k, as illustrated in Figure 2f. Its magnitude is commonly quantified by a parameter α which is the ratio between the amplitude of the band splitting and the corresponding displacement away from the high symmetry point ($\alpha = \Delta E/2k_R$).[35,84] The symmetry breaking displaces the valence band maximum and/or conduction band minimum from the symmetry points in the Brillouin zone, giving rise to the Rashba or Dresselhaus effect (Figure 2g,h).[84] These effects may manifest individually or coexist in materials with the site or bulk inversion asymmetry.[84,85] With the integration of chiroptical properties, photoinduced spin-charge interconversion in chiral metal halides with spin-splitting could provide a route to optically controlled spintronics without the use of external magnetic fields.[81,85,86]

2.1.4. Other Mechanisms

Recent studies have unveiled a range of novel mechanisms for CP light detection in chiral metal halides. While they collectively leverage crystal asymmetry, their underlying physical origins and operational principles are distinct, offering a versatile platform for high-performance, self-powered CP discrimination.

The circular photogalvanic effect (CPGE) originates from SOC induced asymmetric carrier distribution in k-space. It directly generates a helicity-dependent photocurrent whose direction reverses sign upon switching the CP light handedness, without an external bias.[87] In contrast, the bulk photovoltaic effect (BPVE) and the closely related anomalous photovoltaic effect (APVE) are bulk effects arising from both intrinsic crystal polarity and noncentrosymmetry. The BPVE allows the photocurrent direction to be templated by chiral cations,[88] while the APVE is specifically characterized by its ability to generate a steady photocurrent and above-bandgap photovoltage.[89–93] The chiral-polar photovoltaic effect (CPPE) represents an advanced manifestation of these bulk effects, uniquely integrating chiral spin selectivity with polar charge separation. This synergy enables highly sensitive self-powered detection by simultaneously suppressing dark current and enhancing spin-polarized transport.[19,37,88,94–98] Diverging from these electronic processes, the pyro-phototronic effect operates on a light-thermal-electric pathway. It exploits differential CP absorption to create asymmetric heating, which generates a pyroelectric current and an internal field that further facilitates charge separation.[99,100] These mechanisms illustrate a rich landscape of chiroptoelectronic phenomena, each providing a unique strategy for CP light detection. It is worth noting that the origins of material chirality will be further discussed in Section 4.

2.2. Quality Factors of CP Photodetectors

CP photodetectors share fundamental performance metrics with conventional photodetectors, including responsivity (R_λ), specific detectivity (D^*), external quantum efficiency (EQE), etc. Their distinguishing capability lies in differential signal generation for LCP light versus RCP light, quantified through anisotropy factors such as the anisotropy factor of photocurrent (g_{Iph}) and the anisotropy factor of responsivity (g_{res}).

2.2.1. The Anisotropy Factor of Photocurrent (g_{Iph})

One of the specific performance metrics of CP photodetectors is the g_{Iph} which represents the distinguished photocurrent ability between LCP and RCP light. Based on the photocurrent values measured under LCP and RCP light (I_{LCP} and I_{RCP}), the g_{Iph} (which is also expressed by g_{ph} in some literatures) is defined as:

$$g_{Iph} = 2 \times \frac{I_{LCP} - I_{RCP}}{I_{LCP} + I_{RCP}} \tag{8}$$

In an ideal system with perfect CP light discrimination, the value of g_{Iph} is ±2.

2.2.2. The Anisotropy Factor of Responsivity (g_{res})

In analogy to the g_{lph}, the g_{res} is defined as:[20]

$$g_{res} = 2 \times \frac{R_{LCP} - R_{RCP}}{R_{LCP} + R_{RCP}} \tag{9}$$

where R_{LCP} and R_{RCP} are the responsivity under LCP and RCP light illumination, respectively.

2.2.3. Responsivity (R_λ)

The R_λ reflected the device response sensitivity to incident light, calculated as:[101]

$$R_\lambda = \frac{I_{photo} - I_{dark}}{P_\lambda \cdot S} \tag{10}$$

where I_{photo} and I_{dark} represent the photocurrent and dark current, P_λ is the light power density at a particular wavelength (λ), and S is the effective illumination area of the device.

2.2.4. Specific Detectivity (D*)

Another key sensor parameter for photodetectors is D^*, which is not only related to response of the device under illumination but also corresponding with the current signal in dark state, given by the equation:[102]

$$D^* = \frac{R_\lambda \sqrt{S}}{\sqrt{2qI_{dark}}} \tag{11}$$

where q is the electron charge.

2.2.5. External Quantum Efficiency (EQE)

The EQE quantifies a photodetector's photon-to-electron conversion capability, defined as:

$$\mathrm{EQE} = \frac{hc}{q}\frac{R_\lambda}{\lambda} \tag{12}$$

where h is Planck's constant and c is the light speed.

2.2.6. Response Speed

Response speed is typically measured by the rise time (τ_r) and decay time (τ_d), defined as the time interval for the photodetector's electrical output signal to transition between 10% and 90% (for τ_r) or 90% and 10% (for τ_d) of its maximum steady-state value.

2.2.7. Bandwidth

Bandwidth (usually specified as -3 dB bandwidth) defines the range of signal frequencies a detector can handle. It is the modulation frequency at which the response is half of the initial value obtained under continuous illumination. A higher bandwidth indicates the detector can process faster, more rapidly varying light signals.

3. Structure and Synthesis of Chiral Metal Halides

Chiral-sensitive materials exhibiting CD offer a promising route for naturally distinguishing LCP and RCP light through their intrinsic optical activity.[72] Although chiral lanthanide complexes and organic molecules possess such capabilities, their complex synthesis and inherently low carrier mobility hinder their practical use.[103] In contrast, chiral metal halides—particularly HMHs—have emerged as strong candidates for CP light detection.[19,72]

Ternary metal halides generally follow the chemical formula AMX_3, where A is a monovalent ammonium cation, M is a divalent metal ion (e.g., Pb^{2+} or Sn^{2+}) or a mixed-valence cation pair (e.g., Ag^+-Bi^{3+}), and X is halogen anion. This composition forms what is commonly referred to as a standard perovskite structure. Within this structure, $[MX_6]^{4-}$ octahedral cavities share corners to form a continuous 3D network, with A-site cations occupying the interstitial spaces in between.[104] When the A-site cation is an organic species, or a mixture of organic and inorganic ligands, the material transitions to a HMH. The integration of both organic and inorganic structural units provides HMHs with a unique combination of low-temperature, solution-processable fabrication and excellent optoelectronic properties, including high optical absorption coefficients, superior carrier mobility, and long carrier diffusion lengths.[41,105] Crucially, structural asymmetry arising from chiral Sohncke space groups can be engineered through various approaches, including intra-crystal chiral configurations, interfacial lattice distortions, and beyond-crystal design strategies.[19,40] These manipulations have enabled remarkable functionalities based on the Neumann-Curie principle, such as nonlinear optics, ferroelectricity, and opto-spintronics, positioning chiral HMHs (CHMHs) as a versatile platform for advanced direct CP light detection applications.[20,56]

3.1. Structural Framework of CHMHs

The successful incorporation of chirality into HMHs was reported as early as 2003.[45,46] However, their optical and chiral properties remained largely unexplored until 2017, with research on direct CP light photodetectors emerging only in 2019.[20,47] These milestones are primarily enabled by the intrinsically flexible lattice structure of HMHs, allowing for the direct embedding of chiral organic ligands into the inorganic framework, which is the most straightforward strategy to induce chiral crystal structures and achieve high CP light detection sensitivity.[20,48] Furthermore, through rational design of chiral functional groups, precise control over crystallographic symmetry, and optimization of processing conditions, the chirality of these systems can be controllably assembled, transferred, and amplified, which will be discussed in detail in Section 4.1.[47,106] Collectively, these integrated strategies provide a solid material foundation for advancing the multifunctional development of CHMH-based optoelectronic devices.

A wide range of chiral organic cations have been employed as A-site components in CHMHs, including 1-(2-naphthyl)ethylamine (NEA), α-methylbenzylamine (MBA, also referred to as α-PEA in some literature), 1-phenylpropylamine (PPA), β-methylphenethylamine (β-MPA), 1-methyl-3-phenylpropylamine (MPPA), *N,N'*-bis(phenylmethyl)-1,2-

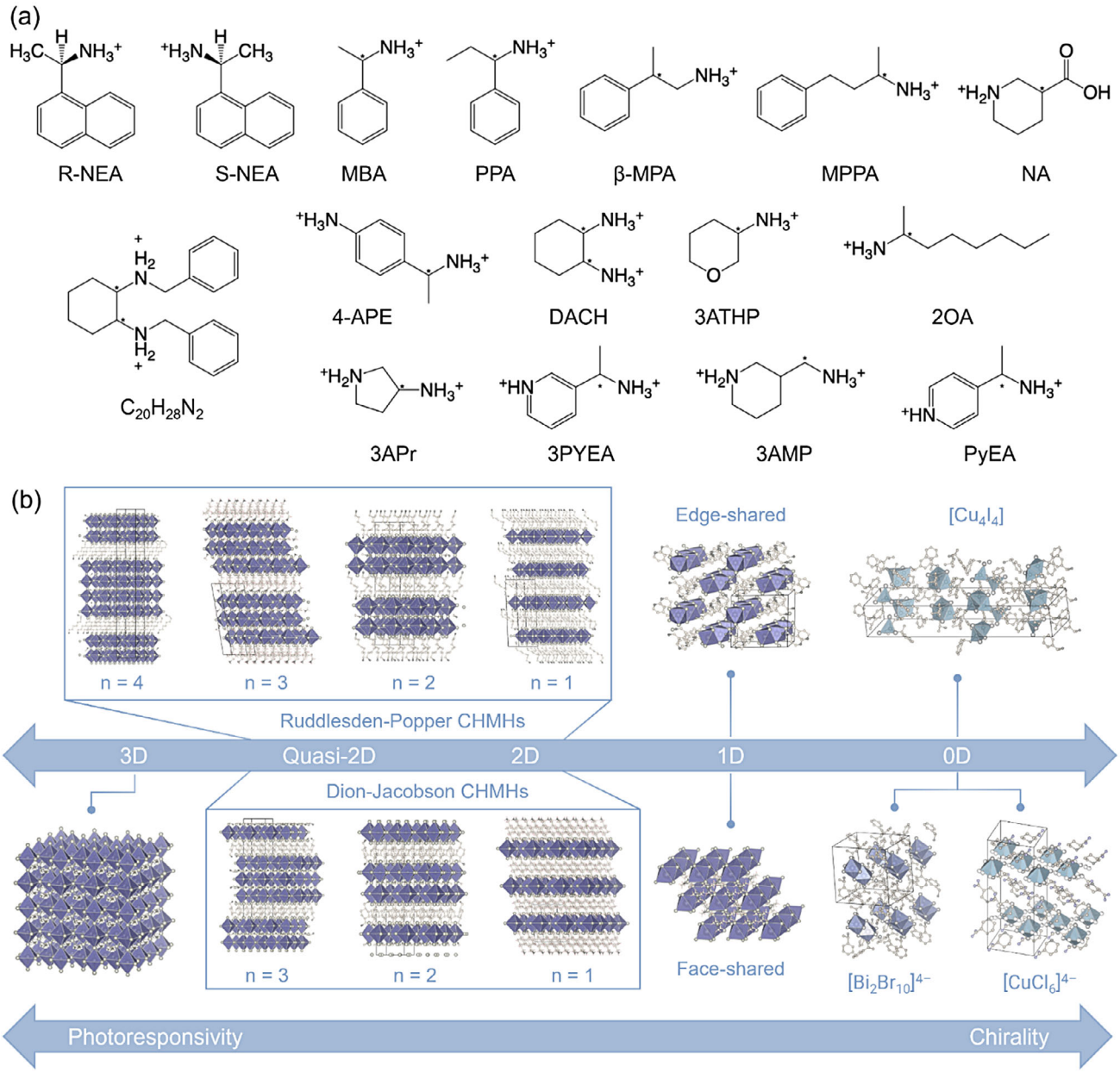

Figure 3. a) Representative chiral organic ligands reported.[24,28,49,99,107–116] b) Crystal structures of CHMHs with varying lattice dimensionalities from 3D, quasi-2D, 2D, 1D to 0D.

cyclohexanediamine ($C_{20}H_{28}N_2$), nipecotic acids (NA), 4-(aminophenyl)ethylamine (4-APE), 1,2-diaminocyclohexane (DACH), tetrahydro-2H-pyran-3-ammonium (3ATHP), 2-octylamine (2OA), 3-aminopyrrolidine (3APr), 1-(3-pyridyl)ethanamine (3PYEA), 3-(aminomethyl)-piperidine (3AMP), and 1-(pyridine-4-yl)ethan-1-amine (PyEA), designated as R- or S-enantiomers based on their handedness (**Figure 3a**).[24,28,49,99,107–116] Due to their bulky molecular size—comparable to the achiral phenylethylamine (PEA) commonly used to substitute smaller cations like methylammonium (MA) and formamidinium (FA)—these chiral cations tend to inhibit the formation of 3D perovskite structures, leading to the emergence of lower-dimensional phases. The resulting architectures consist of self-assembled multiple quantum wells formed by alternating $[MX_6]^{4-}$ octahedra and chiral organic layers, where intrinsic chirality arises from asymmetric hydrogen bonding interactions.[24,117,118] Notably, while these low-dimensional phases feature octahedral units and possess electronic structures resembling those of standard halide perovskites, they should not be simply classified as chiral perovskites, but rather as CHMHs.[119]

Figure 3b presents the crystal structures of CHMHs with varying lattice dimensionalities, as summarized in **Table 2**. Among these, 0D CHMHs, composed of completely isolated

Table 2. Dimensional comparison of CHMHs.

Dimension	Representative formula	Structural features	Property comparison
0D	R_2MX_4 $R_4M_4X_4$ $R_4M_2X_{10}$ $RMX_4{\cdot}H_2O$	Fully isolated metal-halide clusters with strong lattice distortions	Strong chiroptical activity
1D	$RPbX_3$ R_3PbX_5	Metal-halide chains with helical distortion along carrier transport direction	Strong chiroptical activity; efficient carrier migration along chains
2D/quasi-2D (RP type)	$R_2A_{n-1}M_nX_{3n+1}$	Layered structure; helical distortion confined within interlayers	Moderate chiroptical activity; enhanced carrier transport and stability
2D/quasi-2D (DJ type)	$R'A_{n-1}M_nX_{3n+1}$	Diammonium ligands bridge layers; stronger interlayer coupling than RPs	
3D	Standard AMX_3	Conventional 3D perovskite framework; challenging to directly template chirality	Weak chiroptical activity; broad response; high carrier transport

metal halide clusters, exhibit the strongest lattice distortions. This behavior is primarily attributed to the higher molar ratio of chiral components, which enhances the asymmetry of the local coordination environment, resulting in excellent CP light discriminability. These distorted, disconnected clusters are typically templated by bulky chiral ligands and involve diverse metal centers, including copper, bismuth, manganese, and cadmium. Representative 0D CHMHs include (R/S-MBA)$_2$CuCl$_4$, (R/S-NA)$_2$CuBr$_4$, (R/S-MBA)$_4$Cu$_4$I$_4$, (R/S-MBA)$_4$Bi$_2$Br$_{10}$, (RR/SS-$C_{20}H_{28}N_2$)MnBr$_4{\cdot}$H$_2$O, and (R-MPPA)$_2$CdCl$_4$.[29,114,116,120–122]

Similarly, 1D CHMHs, composed of face-, edge-, or corner-sharing metal halide chains, also demonstrate notable chiroptical activity and improved photophysical properties, such as (R/S-MBA)PbBr$_3$, (R/S-NEA)PbI$_3$, and (R/S-3ATHP)$_3$PbCl$_5$.[19,33,115] The chiral organic cations tightly wrap around and directly interact with inorganic octahedral chains, imposing strong stereochemical constraints on 1D CHMHs. This interaction induces pronounced distortions in the inorganic chain conformation and strengths organic-inorganic coupling. The resulting helical distortion propagates along the carrier transport direction, enabling efficient and directional migration of photogenerated carriers. Consequently, the absorption difference of CP light is directly converted into electrical signals, leading to outstanding chiroptical effects.[33]

However, achieving high-performance CP light detection requires not only handed optical absorption but also favorable semiconducting properties.[103] While 1D CHMHs excel in chiroptical response, their semiconducting characteristics remain limited. In this regard, 2D and quasi-2D CHMHs stand out as promising alternatives due to their superior optoelectronic properties. These layered CHMHs typically follow the $R_2A_{n-1}M_nX_{3n+1}$ formula, where R is chiral organic ligands, and n denotes the number of $[MX_6]^{4-}$ octahedral sheets sandwiched between organic layers. In 2D CHMHs, however, the rigid corner-sharing inorganic planes confine chiral cations to the interlayer region, spatially restricting their influence and thereby limiting helical distortion compared with 1D counterparts. Moreover, carrier transport and chiroptical response are suppressed because carriers in 2D structures must traverse insulating organic layers aligned parallel to the substrate.

When $n = 1$, the material is classified as a pure 2D CMHM; for $1 < n < \infty$, it is considered quasi-2D; and as n approaches infinity, the system progressively converges to a 3D perovskite. Despite that the chiroptical activity tends to diminish with increasing n due to the reduced proportion of chiral organic ligands, quantum confinement-induced deep-level defects in low-n structures are significantly suppressed in higher-n systems.[123,124] This reduction in carrier recombination traps facilitates more efficient energy transfer and improved optoelectronic conversion efficiency.[125]

In addition to the widely studied Ruddlesden-Popper (RP) type CHMHs discussed above, Dion-Jacobson (DJ) type CHMHs with the general formula $R'A_{n-1}M_nX_{3n+1}$ have also shown explored for CP light detection. Here, R' represents diammonium chiral cations (e.g., 3APr, 3PYEA, and 3AMP), which bridge adjacent inorganic sheets at both sides, eliminating van der Waals gap. This structural feature further weakens both quantum and dielectric confinement effects, thereby enhancing charge transport, optoelectronic conversion, and structural stability.[24,28,113]

Compared with their low-dimensional counterparts, 3D CHMHs offer stronger anisotropic factors and broader CP light response extending to the long-wavelength visible and NIR regions. However, their intra-crystal development remains limited by the scarcity of suitable chiral precursors capable of templating 3D chiral framework (e.g.,PyEA).[49] Consequently, alternative design strategies focus on tuning intrinsic centrosymmetric achiral point group, as discussed in Section 4.3.

3.2. Synthesis Strategies for CHMHs

3.2.1. Single-Crystalline Bulks

Given that the solubility of most ionic compounds decreases with temperature, cooling crystallization has become the most conventional method for synthesizing bulk single-crystalline CHMH.[56] Typically, raw materials containing chiral ammonium cations, metal ions, and halogen ions are dissolved in concentrated hydrohalic solvents (e.g., hydroiodic acid (HI)), followed by thorough stirring at elevated temperature. High-quality crystals are then obtained through a gradual cooling process, as illustrated in **Figure** 4a-i.[20,25,126] Recently, several advanced strategies have been proposed for CHMH synthesis, such as room-temperature slow-volatilization crystallization, which simplifies

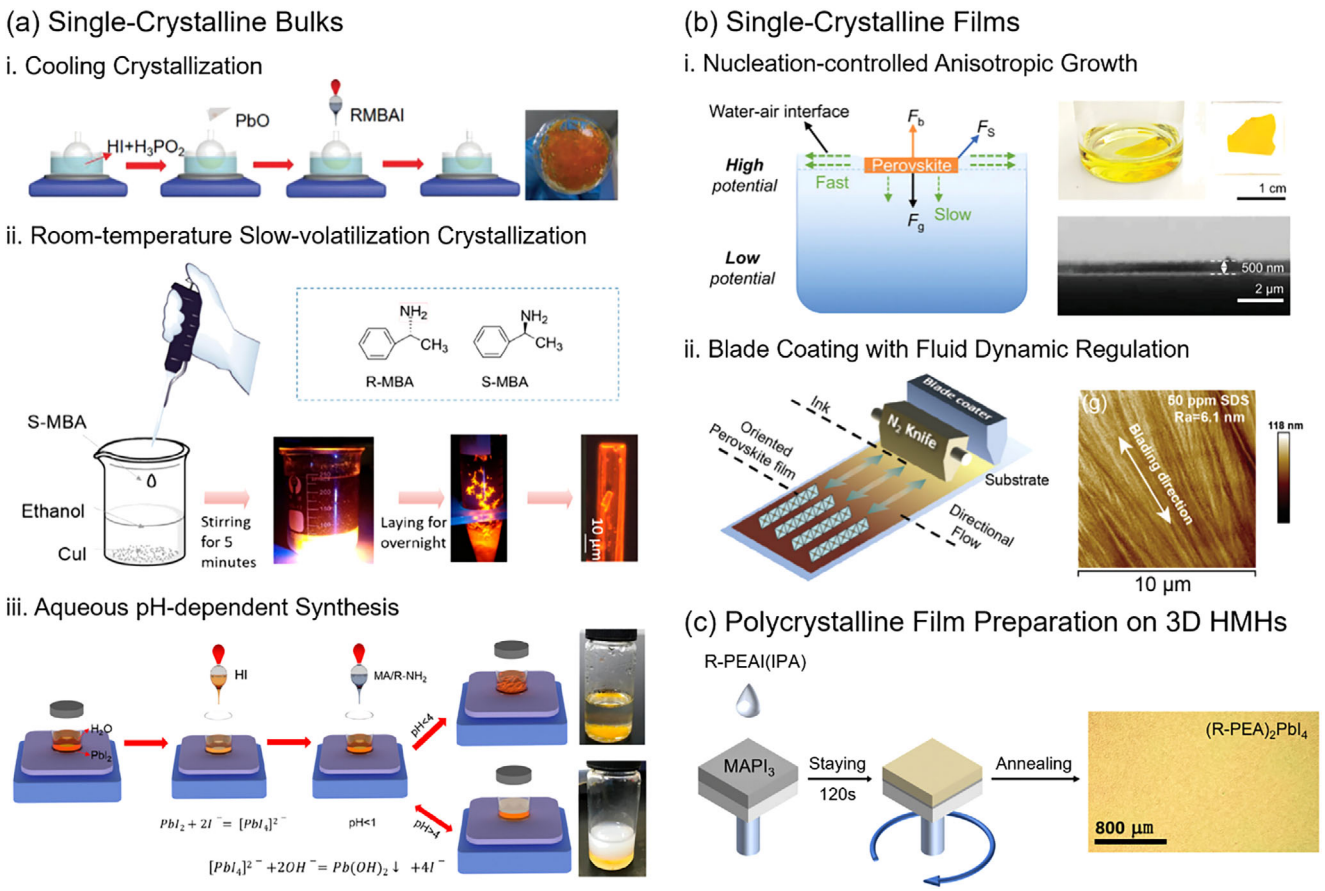

Figure 4. Fabrication approaches for CHMHs in a) single-crystalline bulk. Reproduced with permission.[120,126,128] Copyright 2021, Wiley-VCH. Copyright 2020, American Chemical Society. Copyright 2019, American Chemical Society. b) single-crystalline film,[21,24] and c) polycrystalline film morphology. Reproduced with permission.[129] Copyright 2025, Wiley-VCH. Copyright 2024, Wiley-VCH. Copyright 2023, The Royal Society of Chemistry.

the reaction process,[120,127] and aqueous pH-dependent synthesis, which reduces energy consumption and minimizes the use of toxic solvents, as shown in Figure 4a-ii,iii.[128]

3.2.2. Single-Crystalline Films

Despite the advantageous low-defect nature and high orientation of bulk single-crystalline CHMH, their limited flexibility in design and functional integration poses challenges for photodetection applications. In contrast, single-crystalline films, which retain superior crystallization quality while offering enhanced processability, show great promise to device fabrication. These films can be readily prepared by dissolving pre-synthesized single crystals in polar solvents (e.g., *N,N*-dimethylformamide (DMF), dimethyl sulfoxide (DMSO)) followed by spin-coating.[20] To further enhance the area and aspect ratio of single-crystalline films, a nucleation-controlled strategy was proposed for (R/S-3APr)PbI_4 crystallization, as depicted in Figure 4b-i. Driven by surface tension and buoyant forces, precursor molecules self-assemble at the liquid-gas interface, leading to elevated chemical potential and accelerated anisotropic growth of CHMH films in the horizontal direction. Consequently, as-grown (R/S-3Apr)PbI_4 films achieve centimeter-scale widths with submicron thickness, offering significant potential for large scale device array construction.[24]

In 2024, an innovative method was introduced for fabricating uniaxially oriented (R/S-NEA)PbI_3 films through fluid dynamic regulation during the blade coating process, as shown in Figure 4b-ii. By incorporating versatile surfactants, surface tension gradients spanning from the contact line to the meniscus can be effectively minimized, facilitating controlled Marangoni flow for balanced mass transport. This approach promotes the high-quality growth of oriented CHMH crystals with reduced trap density and efficient charge carrier collection, resulting in an exceptional g_{CD} of 0.042. Consequently, the integrated CP photodetector—here referring to a device in which oriented CHMH films are structurally incorporated into a complete architecture—exhibits a tenfold improvement in detectivity and enhanced g_{Iph} from 0.45 to 0.70 compared to the surfactant-free (non-oriented) device.[21]

3.2.3. Polycrystalline Films

Compared to their single-crystalline counterparts, polycrystalline CHMH films offer a more straightforward fabrication route via spin-coating, using precursor solutions containing chiral organic

halide salts.[130,131] The orientation of polycrystalline films can be effectively regulated by adjusting parameters such as precursor concentration, solvent type, and annealing temperature.[47] Due to the outstanding compatibility with both rigid and flexible substrates, combined with great potential for scalable preparation, this solution-processable approach has been widely demonstrated across various photonic and electronic applications.[86] Recently, an innovative intermittent spin-coating strategy was introduced for fabricating CHMHs directly on the surface of 3D HMH films. As demonstrated in Figure 4c, an isopropanol solution containing the chiral ligand R-MBAI is spin-coated onto pre-formed 3D $MAPbI_3$ films, converting its top surface into 2D CHMHs. By tuning the concentration of R-MBAI, a thicker chiral layer can be formed on the surface, while preserving a thinner 3D layer underneath. Meanwhile, compared to conventional multi-step spin-coating, the intermittent approach provides sufficient time for the chiral ligand to diffuse into the film, allowing for a more effective incorporation of the chiral phase without compromising film quality. This method offers a promising and scalable strategy for the fabrication of high-performance CP light photodetectors.[129]

4. Manipulation of Chiral Optical Fields in Different Metal Halides

Tailoring CP light-matter interactions at the molecular and mesoscale dimensions has been increasingly pursued as a promising approach for the manipulation of chiral optical fields. In CHMHs, this is achieved through several well-established chirality-transfer mechanisms: 1) chiral organic molecules inducing chiral inorganic structures; 2) chiral distortion of inorganic surfaces; 3) electronic coupling between chiral ligands and achiral inorganic frameworks; and 4) chiral self-assembly at the supramolecular level. These mechanisms enable the breaking of inversion symmetry and introduction of structural handedness via atomic-scale lattice distortion, surface patterning, or long-range chiral ordering. A variety of structural and compositional modulation techniques have been developed to harness these mechanisms, systematically engineered across different hierarchical levels—including intra-crystal chiral configuration, interfacial lattice distortion, and beyond-crystal chiral superstructures—these methodologies constitute a multiscale framework for the rational modulation of chiroptical responses across diverse classes of HMHs.

4.1. Intra-Crystal Chiral Configuration

At the most fundamental level, chirality can be embedded directly within the crystal lattice. Such intra-crystal chiral configuration arises from the incorporation or induction of chirality at the atomic or molecular scale, where the arrangement of intrinsic lattice sites (i.e., A-, M-, and X-sites) together with extrinsic factors such as additives, pressure, or templating induces asymmetric bonding and lattice distortions that strongly couple with the electronic structure, thereby laying the foundation for higher-order chiroptical control.

4.1.1. A-Site Cation Engineering

In CHMHs, chirality primarily originates from chiral organic spacer cations located at the A-site, intercalated between inorganic layers. With identical dimensionality and halide composition, variations in A-site cations can significantly modulate anisotropy factors in CP light detectors.[61] Therefore, rational A-site cation design is a pivotal strategy to enhance chiroptical responses. This section outlines four strategic approaches for boosting chiroptical responses through A-site engineering: functional group substitution, chiral-chiral cation mixing, achiral cation incorporation, and polymerizable cation adoption.

Functional group substitution significantly influences chiroptical properties by altering hydrogen bonding and molecular packing.[132,133] For example, shifting the amino group position in naphthyl-ethylamine isomers leads to substantially different CD signals ($g_{CD} = 2.01 \times 10^{-3}$ vs. -2.78×10^{-3}), resulting from differential penetration depth of NH^{3+} groups and consequent conformational reorganization of the organic moieties.[134] Halogen type and position also critically modulate chiroptical response through both steric and electronic effects.[135,136] Ortho-fluorination in $(S\text{-}2F\text{-}MBA)_2PbI_4$ induces stronger F···I interactions and asymmetric NH···I bonding, yielding a high g_{CD} of 1.68×10^{-3} and g_{Iph} of 0.288.[137,138] Similarly, ortho-chlorinated spacers achieve a remarkable g_{Iph} of 1.25 in $(R/S\text{-}o\text{ClMBA})PbI_3$ (oClMBA = 1-(*ortho*-chlorophenyl)ethylamine), attributed to enhanced inorganic framework distortion and the change in dimensionality caused by variations in the nature of hydrogen bonds.[139]

In some CHMH systems, inversion symmetry is disrupted through chirality transfer, while corresponding space groups (e.g., $P2_1$, $P2_12_12_1$, $Pmc2_1$) still retain symmetry elements like screw axes or mirror planes, limiting lattice distortion and further chirality transfer.[79] To address this, a chiral-chiral mixed-cation approach, such as trace doping of S-2-methylbutylammonium (S-2-MeBA) into S-BrMBA, can reduce symmetry from $C2$ to $P1$. This structural transition not only breaks global symmetry but also enables spin-splitting modulation along different k-paths in the Brillouin zone, offering opportunities for enhancing spin-related chiroptical properties.[140] Nevertheless, practical use of this strategy is constrained by the limited availability and synthesis challenges of commercial spacers, with most studies relying on a handful of readily available options like MBA^+ and NEA^+.[139] Thus, more scalable strategies for symmetry engineering and chirality enhancement in CHMHs are urgently needed beyond chiral-chiral cation mixing.

The strategic incorporation of achiral cations provides an effective route to enhance the chiroptical properties and stability of CHMHs by improving chirality transfer through structural optimization and strengthened intermolecular interactions. Introducing achiral alkyl cations into chiral frameworks induces alternating cation intercalation (ACI), which reduces interlayer spacing and strengthens non-covalent interactions. Mixed-cation CHMHs are thermodynamically most stable at 1:1 alkyl-aryl ratio and exhibit significantly enhanced anisotropy factors.[141–145] For example, $(R\text{-}MBA_{0.5}nBA_{0.5})_2PbI_4$ shows a tenfold increase in g_{CD} to 2.89×10^{-3} compared to pure $(R\text{-}MBA)_2PbI_4$.[146] Short-chain alkyl cations (e.g., EA, PA, and BA) with minimal steric hindrance are synthetically tractable.[23,96,98,147,148] As shown in

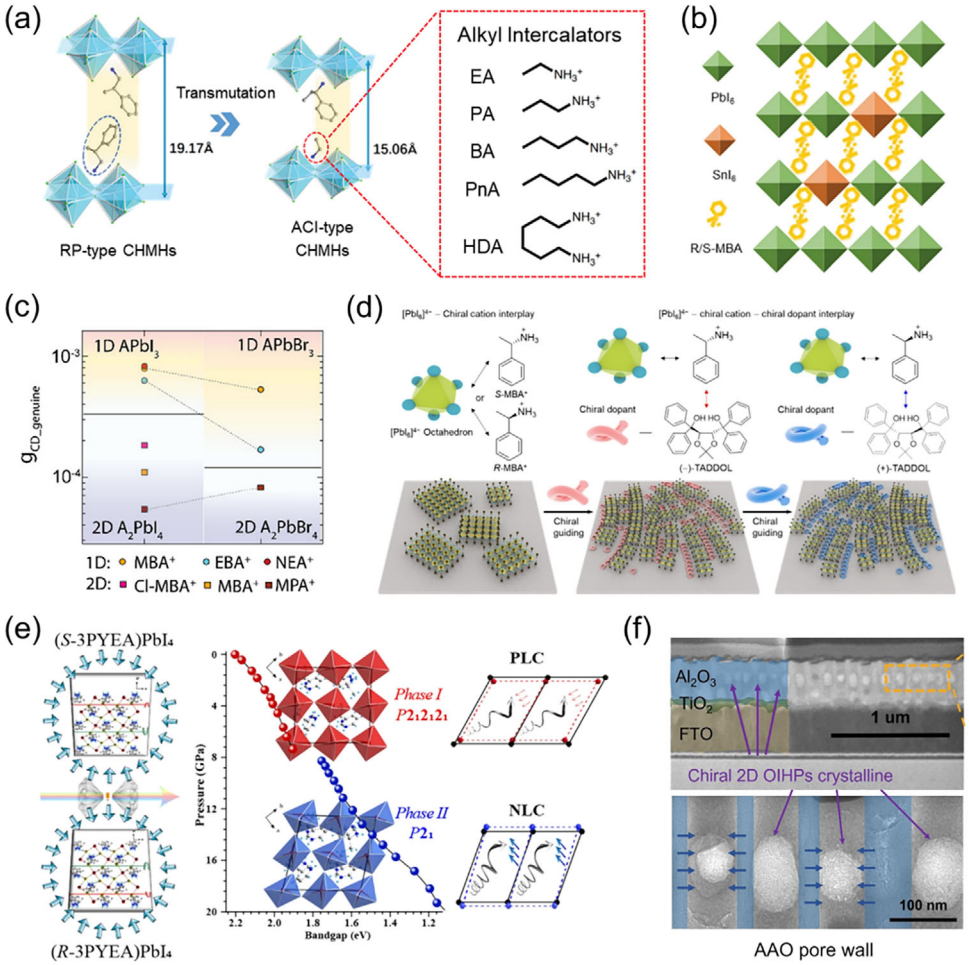

Figure 5. Modulation of chiral optical fields through intra-crystal chiral configuration: a) A-site cation engineering. Reproduced with permission.[98] Copyright 2022, Wiley-VCH. b) M-site cation engineering.[27] Copyright 2023, American Chemical Society. c) X-site cation engineering. Reproduced with permission.[61] Copyright 2022, American Chemical Society. d) Additive engineering. Reproduced with permission.[32] Copyright 2024, American Association for the Advancement of Science. e) Pressure modulation. Reproduced with permission.[113] Copyright 2023, American Chemical Society. f) Spatially confined growth. Reproduced with permission.[153] Copyright 2022, Springer Nature.

Figure 5a, compared to conventional RP configurations, alternating alkyl-aryl intercalation reduces van der Waals forces and interlayer spacing, enhancing intrinsic stability and charge transport efficiency.[98,149] This configuration engages all aryl cations in interlayer interactions—unlike partial participation in pure chiral-cation systems—thereby amplifying chiroptical responses.[141] Incorporating larger achiral cations presents greater challenges but crucial for property tuning. The strategy also extends to diammonium spacers such as hexane-1,6-diammonium (HDA), which reinforce hydrogen-bonding networks and improve device performance.[150] This versatile approach enables scalable enhancement of structural symmetry and chirality transfer for high-performance CP photodetectors.

Compared to saturated chiral cations, unsaturated cations with C=C bonds offer the unique advantage of enabling in situ polymerization. This approach enhances CHMH crystallinity and lattice rigidity, leading to reduced defect formation and improved operational stability.[151] The resulting cross-linked structures also impart mechanical flexibility, facilitating the development of stable, flexible optoelectronic devices and highlighting the promise of polymerizable chiral cations for next-generation CP light applications.[152]

4.1.2. M-Site Cation Engineering

Engineering the M-site in chiral metal halides provides a critical pathway to tailor spin-dependent properties and chiroptical performance. Modulating the central metal cation composition directly influences the SOC strength, electronic band structure, and chirality transfer to the inorganic lattice in chiral metal halides.[154]

Tin (Sn) doping represents a trade-off between Sn incorporation and chiroptical activity (Figure 5b).[155] Low to moderate Sn incorporation (5–10%) in Pb-based CHMHs exhibit optimal g_{CD} ($\approx 1.5–1.6 \times 10^{-3}$), comparable to the pristine (R/S-MBA)PbI_4 (1.8×10^{-3}). However, higher doping levels (>20%) sharply reduce g_{CD} to below 0.5×10^{-3}. Sn incorporation reduces symmetry from

$P2_12_12_1$ to $P1$, which strengthens spin splitting near the valence band maximum (VBM), narrows the bandgap and extends the optical response to ≈600 nm, enabling broader CP light detection coverage into the visible-NIR range.[27,156]

Alternatively, lead-free strategies have gained attention for their eco-friendly potential and unique structural advantages. Ag-Bi bimetal CHMHs, for instance, exhibit chiral polar crystal structures together with pronounced bulk photovoltaic effects, allowing self-powered CP light detection with competitive anisotropy factors.[127] Similar approaches have been successfully extended to other lead-free metal halides, highlighting the importance of balanced charge distribution and steric compatibility as key design principles for developing high-performance "green" CHMHs.[29,72,94,157–160]

4.1.3. X-Site Halide Engineering

Compared with A- or M-site engineering, X-site halide substitution in CHMHs primarily modulates the chiroptical response wavelength due to its direct influence on electronic structure. In Pb-based CHMHs, the CBM derives from Pb 6p orbitals and the VBM from Pb 5s-halide p hybridization. Since Br 4p has a lower energy level than I 5p, replacing iodide with bromide widens the bandgap, where tuning Br content in $(R/S\text{-}MBA)_2PbI_{4(1-x)}Br_{4x}$ shifts responses from 496 nm ($x = 0$) to 455 nm ($x = 0.5$).[161] However, halide mixing often induces a phase transition from chiral $P2_12_12_1$ (iodine-dominant) to achiral (bromide-dominant), reducing CP light responsivity below 474 nm due to phase separation or low-chirality mixed phases.[47] As Br fully substitutes I, however, $|g_{CD}|$ of $(R/S\text{-}MBA_{0.75}PEA_{0.25})_2PbI_{4(1-x)}Br_{4x}$ increases above 3.8×10^{-3}.[145] For 1D CHMHs with identical dimensionality and cations, lead iodide series $RPbI_3$ consistently display higher genuine anisotropy factors than bromide counterparts ($RPbBr_3$), as demonstrated in Figure 5c. This is because, despite similar exciton spacing, bromide-based CHMHs possess higher binding energy and thus smaller dipole moments, leading to weaker long-range dipole-dipole coupling and reduced CD intensity compared with iodide series.[61]

4.1.4. Additive Engineering

Additive engineering serves as an effective synthetic strategy to modulate crystallization kinetics, suppress defects, and enhance the chiroptical performance of chiral metal halide thin films. The introduction of volatile or nonvolatile additives enables precise control over film morphology, phase distribution, and chiral order. Volatile Lewis bases, such as methylammonium thiocyanate (MASCN), regulate crystallization by temporarily coordinating with metal ions and organic moieties, thereby improving crystallinity, reducing trap states, optimizing phase distribution, and grading band alignment.[162–164] In contrast, nonvolatile additives like urea remain embedded in the lattice after processing, sustaining robust Lewis interactions that induce further conformational distortion and amplify chirality.[130,165]

Beyond monolithic chiral organic cation-inorganic frameworks, incorporating external chiral dopants is an effective way to enhance CHMH chiroptical properties. For instance, surface passivation of $(R/S\text{-}MBA)_2FA_2Pb_3Br_{10}$ with excess chiral amine R/S-MBABr improves film quality and structural asymmetry, leading to an increase in CP light response by 30%.[166] Chiral dopants, such as (2R,3R/2S,3S)-2,3-O-isopropylidene-1,1,4,4-tetraphenyl-1,2,3,4-butanetetrol (R/S-TADDOL), drive crystal reconstruction through π–π stacking and hydrogen bonding, effectively extending the helical chirality of the inorganic framework and enhancing long-range chiral order (Figure 5d).[32,167,168] This leads to significantly amplified chiroptical responses, with g_{Iph} exceeding 1.1 in self-powered CP light photodetectors.

4.1.5. Other Modulation Strategies

Beyond chemical composition tuning, physical and spatial modulation strategies offer alternative routes to enhance the chiroptical properties of chiral metal halides. These approaches manipulate crystal structure and molecular packing through external stimuli or confinement effects, providing complementary insights into chirality control. High-pressure processing induces structural phase transitions and enhances asymmetric hydrogen bonding, leading to amplified chiral asymmetry.[169,170] For example, DJ-type $(R/S\text{-}3PYEA)PbI_4$ undergoes an orthorhombic-monoclinic transition at ≈7.0 GPa with band-gap redshift and pronounced piezochromism, as illustrated in Figure 5e. Further compression induces chirality-driven negative linear compressibility along the *c*-axis, caused by homo-directional tilting of R/S-$3PYEA^{2+}$ and intensified asymmetric hydrogen bonding. These effects distort the $[PbI_6]^{4-}$ octahedra and enhance chiral asymmetry, enabling $(R/S\text{-}3PYEA)PbI_4$ to achieve improved CP light distinguishability and strong NIR absorption, making it promising for high-performance NIR-CP light detectors.[113] Spatial confinement within nano-templates (e.g., anodized aluminum oxide (AAO)) generates micro-strain that modifies molecular stacking and strengthens π-p orbital coupling, resulting in significantly enhanced dissymmetry factors with $|g_{CD}|$ improvements exceeding fivefold (Figure 5f).[153,171]

4.2. Interfacial Lattice Distortion

As discussed in Section 4.1, the chirality of state-of-the-art CHMHs primarily originates from the direct incorporation of bulky chiral organic spacer cations. However, the structural compatibility between these chiral cations and the inorganic metal halide framework, along with considerations of commercial availability and cost, significantly limits the selection of suitable candidates.[141] To overcome these limitations, a novel approach termed "remote chirality transfer" has been proposed, which involves controlling interfacial lattice distortion to impart chirality onto originally achiral metal halides.

This strategy starts from employing post-synthetic ligand treatments on achiral perovskite nanocrystals (NCs), capitalizing on their numerous surface ionic vacancies and dangling bonds, which readily coordinate with chiral organic amines.[56] For instance, introducing a trace amount of chiral R/S-MBABr ligands onto the surface of achiral $FAPbBr_3$ NCs was shown to not only induce structural chirality but also significantly reduce nonradiative recombination, as shown in **Figure 6a**.[172] Subsequent

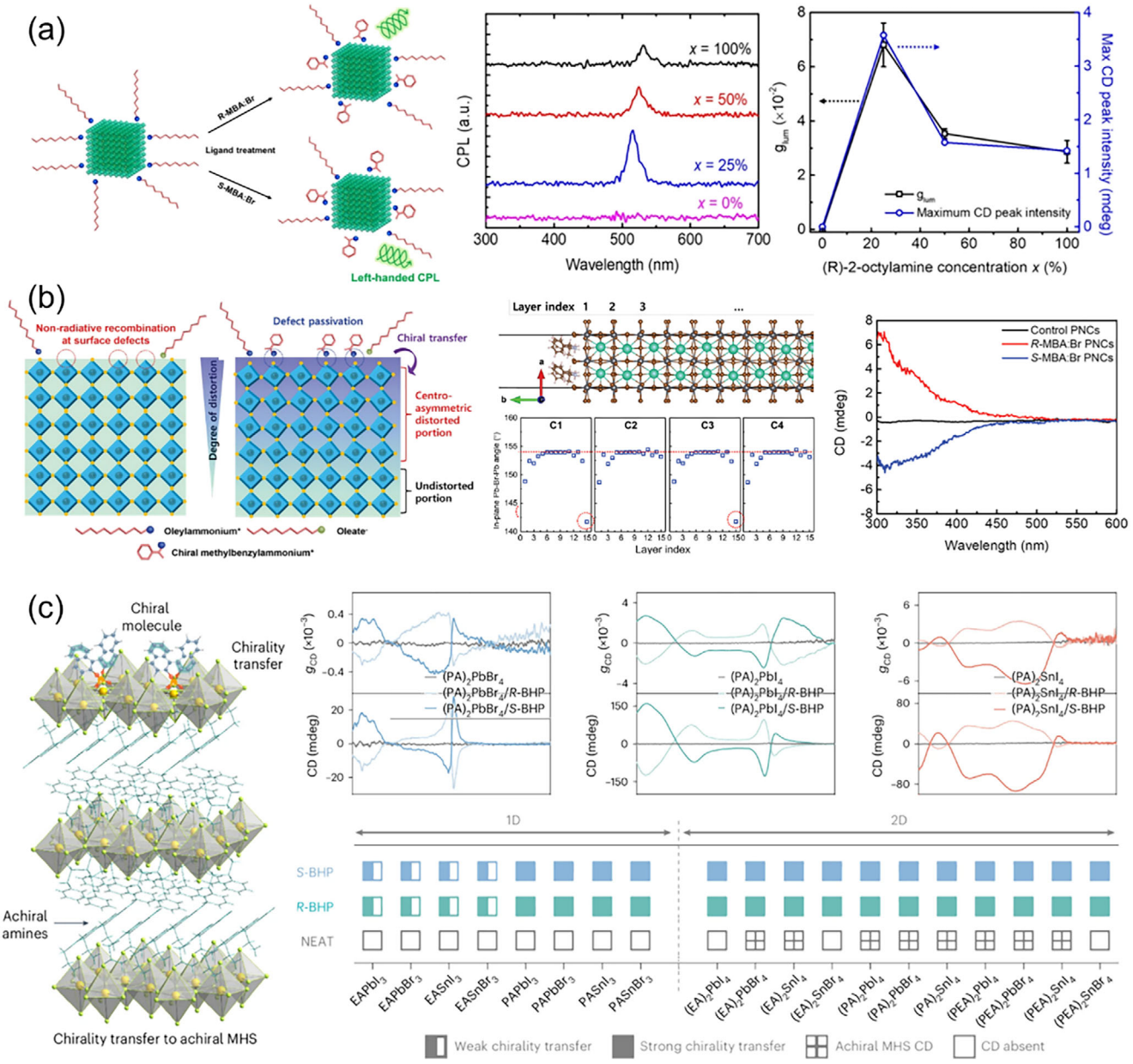

Figure 6. Remote chirality transfer for interfacial lattice distortion-induced chirality generation: a) Primary exploration on achiral $FAPbBr_3$ NCs. Reproduced with permission.[172] Copyright 2020, American Chemical Society. b) Mechanism study based on R/S-MBA-modified $CsPbBr_3$ NCs. Reproduced with permission.[76] Copyright 2022, Wiley-VCH. c) Further application to diverse low-dimensional HMH thin films. Reproduced with permission.[173] Copyright 2025, Springer Nature.

studies have further validated the broad applicability of this method across diverse perovskite systems, including achiral all-inorganic $CsPbX_3$ (X = Cl, Br, and I) perovskites with various chiral amines such as NEA, DACH, and 2OA.[107–109]

To elucidate the mechanism by which chiral surface ligands impart chiroptical responses to achiral perovskites, detailed studies have been conducted using R/S-MBA-modified $CsPbBr_3$ NCs, as shown in Figure 6b. Density function theory (DFT) simulations reveal that adsorption of chiral ligands triggers centro-asymmetric distortions of the inorganic $[PbX_6]^{4-}$ octahedra. These distortions propagate through multiple inorganic atomic layers (up to fifth outermost plane), thereby effectively inducing structural chirality onto achiral perovskite lattices.[76]

Although chirality transfer induced by interfacial chiral ligands in perovskite NCs is relatively well-established, this strategy has primarily been utilized for CP light emission rather than detection, due to inherent structural and dimensional limitations of NCs. The few existing examples of NC-based CP light detection typically rely on heterojunctions with other semiconductor materials (e.g., such as carbon nanotubes) to enhance CP light selectivity.[76] To this end, efforts have expanded this interfacial strategy to HMH systems of varying morphologies. For instance,

HMH nanoplatelets capped with chiral colloidal quantum ligand R/S-MBA as capping ligands were synthesized. This approach leads to the formation of a distinct ligand-metal halide charge-transfer band characterized by excitonic features arising from electronic coupling between ligands and the quantum-confined axis of the nanoplatelets.[174] Further ligand exchange studies using R/S-MPEA (MPEA = β-methylphenethylamine) on colloidal lead bromide nanoplatelets of different layer thicknesses demonstrate that band-edge spin-splitting in these nanoplatelets originates predominantly from ligand-induced symmetry breaking, rather than from direct electronic interactions through hybridized organic-inorganic orbitals.[175]

Moreover, the applicability of "remote chirality transfer" was broadened to include diverse low-dimensional HMHs in thin film morphology. Their systematic study explores various compositional combinations, employing EA, PA, and PEA as A-site cations, lead and tin as B-site components, and iodide and bromide as halide components, as shown in Figure 6c. By carefully adjusting the concentration and chemical nature of the interfacial chiral ligand, specifically R/S-1,1'-binaphthyl-2,2'-diylhydrogenphosphate (R/S-BHP), precise control over the extent of chiral amplification can be achieved. Crucially, the structural chirality imparted through remote chirality transfer results in negligible linear birefringence and linear dichroism, thereby revealing the genuine chiral response of the CHMH systems.[61,134] This flexible strategy eliminates the necessity for extensive internal chiral structural modification, requiring only trace amounts of chiral ligands to achieve significantly enhanced the g_{CD} value (up to $\approx 10^{-2}$), without compromising the intrinsic optoelectronic properties of HMH films.[173]

4.3. Beyond-Crystal Design

It is well established that even without chiral components, chiroptical activity can arise in achiral crystals that belong to certain asymmetric point groups (m, $mm2$, 4, and $42m$), which opens up a vast array of design possibilities that do not rely on intracrystal or interfacial incorporation of chiral molecules.[93,176] In this context, symmetry breaking becomes the key determinant in enabling CP light responsiveness in achiral HMHs. To this end, various "beyond-crystal" strategies have been developed to induce or modulate symmetry-breaking effects and chiroptical response through physical, morphological, and external field engineering.

4.3.1. Structural and Morphological Engineering

Structural and morphological control provides effective means to enhance the chiroptical response of metal halide films and devices through optimized light-matter interaction and symmetry breaking. The ability of a CP photodetector to differentiate LCP and RCP light, expressed as $\Delta n/n$, depends on the thickness (d) of the active layer and can be described by:

$$\frac{\Delta n}{n} \approx \frac{2(n_L - n_R)}{n_L + n_R} \approx \frac{(\alpha_L - \alpha_R)}{\exp(\alpha_L d) - 1} \quad (13)$$

where n_L and n_R represent the carrier concentrations generated by LCP and RCP light, respectively, and α_L and α_R are their corresponding absorption coefficients. Excessively thick layers reduce $\Delta n/n$ and lead to a diminished CP light response, whereas an optimal thickness $\approx 1/\alpha_L$ maximizes chiroptical contrast.[20] This effect was experimentally demonstrated in (R-$MBA_{0.5}nBA_{0.5}$)$_2PbI_4$ (nBA = n-butylammonium) films formed by different precursor concentrations. Compared to the 0.3 M counterpart with the thickness of $\approx$330 nm, 0.2 M (R-$MBA_{0.5}nBA_{0.5}$)$_2PbI_4$ films exhibited lower absorbance and CD signal intensity due to reduced thickness ($\approx$220 nm), while their g_{CD} value increased by $\approx$10% (from 2.64×10^{-3} to 2.89×10^{-3}), indicating optimized chiroptical properties.[146]

Furthermore, the fabrication of micro-/nanowire arrays significantly enhances polarized light sensitivity through anisotropic confinement and improved crystallographic orientation. Capillary-bridge assembly enables scalable integration of aligned nanowires of 2D (R/S-MBA)$_2PbI_4$, increasing the g_{res} from 0.09 to 0.15.[177] This strategy is broadly applicable to various compositions—including 1D (R/S-$C_5H_{14}N$)PbI_3 and 2D/3D halogenated analogues—enabling wafer-scale integration as demonstrated in a 4-inch Si/SiO_2-based 16×16 pixel imaging array with high polarization distinguishability.[49,178–182]

4.3.2. Solution-Process Engineering

Solution-process engineering offers precise control over crystallization kinetics and phase distribution in polycrystalline CHMH films through solvent and antisolvent selection, directly influencing their chiroptical properties. Solvent choice dictates the formation of intermediate complexes (e.g., $[PbI_xS_y]^{2-}$, where S represents solvent molecules and x and y are integers),[183] which subsequently affects nucleation, grain orientation, and organic-inorganic interaction during crystallization.[184] The use of strongly coordinating solvents modulates crystal growth and enhances chirality. For example, pure DMSO slows crystallization and promotes preferential adsorption of chiral cations (e.g., R-β-MPA^+) at nucleation sites via van der Waals interactions, leading to highly oriented growth and enhanced CD signals (**Figure 7a-i**).[22] Similarly, *N*-methylpyrrolidone (NMP) exhibits strong steric hindrance that inhibits nucleation and favors (002)-oriented growth of (R/S-MBA)$_2PbI_4$, while enhanced intermolecular interactions increase lattice distortion and film chirality (Figure 7a-ii).[185] Solvent-induced phase distribution also plays a critical role: acetonitrile (ACN) promotes aligned 1D/2D hybrid phases with higher g_{CD}, whereas DMF favors larger grains and improved charge transport despite lower g_{CD}.[186]

The solvent engineering strategies discussed above are primarily developed for lead-based perovskites. Although reports on non-lead CHMH systems (e.g., Sn^{2+}- or Bi^{3+}-based) are limited, the underlying mechanisms of these strategies are largely analogous, and their structural similarity suggests that comparable modifications can be achieved.[187] Nevertheless, caution is needed; for example, in Sn-based perovskites, certain solvents (e.g., DMSO) can contribute to Sn(II) oxidation, leading to the undesired formation of dimethylsulfide (DMS) and Sn(IV).[188,189] In such cases, a tailored solvent selection is required (e.g., DEF:DMPU).[190]

Antisolvent engineering complements this approach by suppressing intermediate phases and improving phase purity. A series of antisolvents, including chloroform (CF), chlorobenzene

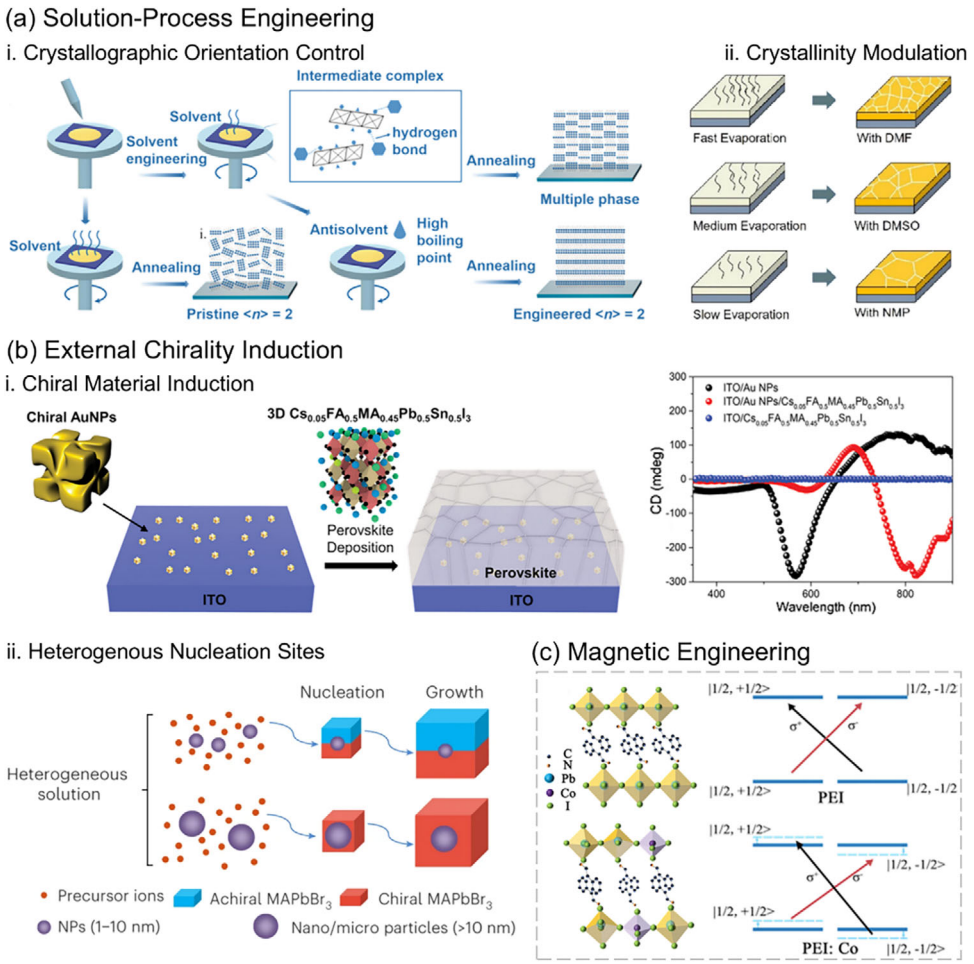

Figure 7. Chirality introduction through beyond-crystal design: a) Solution-process engineering. Reproduced with permission.[22,185] Copyright 2020, Wiley-VCH. Copyright 2023, American Chemical Society. b) External chirality induction. Reproduced with permission.[50,52] Copyright 2022, Wiley-VCH. Copyright 2023, Springer Nature. c) Magnetic engineering. Reproduced with permission.[191] Copyright 2016, Springer Nature.

(CB), diethyl ether (DEE), and toluene (Tol), were applied during the spin-coating process. Among these, CF was identified as the most suitable due to its miscibility with both DMF and DMSO, as well as its superior ability to suppress the formation of undesired intermediate and secondary phases, thereby facilitating direct crystallization of pure-phase CHMHs.[192] This process reduces defects and strengthens hydrogen bonding, inducing symmetry-breaking distortion in the inorganic framework and resulting in a threefold increase in CD intensity.[117] Like solvent engineering, antisolvent engineering, well established in lead-based perovskites, is expected to be transferable to non-lead CHMH systems owing to their similar crystallization behavior. Future development should focus on tailoring antisolvent selection to the specific reactivity of alternative cations, thereby enhancing film quality and chirality transfer ability in emerging CHMHs.

4.3.3. External Chirality Induction

Chiroptical activity in otherwise achiral metal halides can be induced through external chiral influences or localized symmetry breaking rather than intrinsic molecular chirality. Recent advances have explored external chiral material induction as a promising route to endow achiral HMHs with chiroptical activity. Chiral plasmonic Au nanoparticles (AuNPs) with a helicoidal morphology, when embedded into achiral 3D perovskite films, generate pronounced chiroptical responses in the NIR region (Figure 7b-i).[50] This enables high-performance NIR CP photodetection with a g_{res} of 0.55 at 808 nm. Notably, the localized surface plasmonic resonance of AuNPs can be precisely tuned through adjustments in their size, spacing, composition, geometry, and the refractive index of surrounding medium.[193] When the plasmonic resonance aligns spectrally with the absorption profile of HMHs, CP light detection performance significantly improves, enabling its applicability across diverse active-layer HMHs. Similar strategies using other external chiral environments, such as chiral metal-organic frameworks (MOFs) and chiral supramolecular gels, offer an alternative for symmetry breaking and chirality transfer.[107,194,195]

Heterogeneous nucleation sites introduce heterogenous micro- or nanoparticles (e.g., carbon quantum dots, Cu, In_2O_3, SiO_2, $PbCO_3$, and Pb(OH)Br) as nucleation sites to induce

symmetry breaking and chiral phase formation during crystallization. In the $MAPbBr_3$ system, heterogeneous nucleation particles lower the critical free energy for forming chiral tetragonal phase (Figure 7b-ii).[52] Unlike traditional methods, the induced chirality arises from specific chiral arrangements of achiral A-site cations interacting with the $[PbX_6]^{4-}$ framework, forming ordered chiral supercells preferentially nucleated on particle surfaces.[196] This ordered structure yields clear CD signals even from racemic structures under specific incident directions, circumventing conventional symmetry constraints by enabling chirality in both non-centrosymmetric and centrosymmetric crystal frameworks.[176] The resulting chiral $MAPbBr_3$ exhibits a g_{CD} of 4×10^{-3}, with corresponding g_{res} values of 0.39 and 0.38 for CP light photodetectors based on R- and L-$MAPbBr_3$, respectively. Substrate-induced symmetry breaking, exemplified by graphene-templated α-$FAPbI_3$, further enables Rashba spin-splitting and spin-polarized photoconduction, achieving a g_{Iph} of 0.32 through local inversion symmetry breaking within the heterojunction.[197,198]

4.3.4. Magnetic Engineering

Enhancing spin polarization through modulation of internal magnetic fields presents another feasible strategy to address the lack of anisotropic photoresponse in achiral HMHs. To this end, a magnetic engineering strategy using Co^{2+} dopants was introduced, creating a series of $(PEA)_2Pb_{1-x}Co_xI_4$ HMHs with enhanced CP light discrimination capability, as shown in Figure 7c. Specifically, the incorporation of Co^{2+} introduces an internal magnetic field that breaks time-reversal symmetry, lifting the spin-state degeneracy similarly to conventional Zeeman splitting under external magnetic fields.[191] Consequently, CP light illumination induces an imbalanced population distribution among electronic spin states, preferentially populating lower-energy spin bands. This imbalance manifests as a pronounced difference in photoluminescence intensity under RCP and LCP light excitation, significantly enhancing spin polarization. Based on this principle, the Co^{2+}-doped CHMH photodetector exhibits exceptional CP light distinguishability, yielding a remarkable g_{Iph} of 0.41.[199]

Beyond cobalt, other magnetic dopant, including transition metals like Mn^{2+} and rare-earth metals such as Eu^{3+}, have also shown effectiveness in enhancing chiral spintronic behavior.[200,201] Even for intrinsically chiral cation-based CHMHs, magnetic ion doping can further facilitate photon and spin-polarization control, improving anisotropic CP light responses by increasing magnetic transition dipole moments.

5. CP Light Detection Based on Metal Halides

Recent advancements in chiral metal halide-based CP light detection have highlighted the critical role of device architecture innovation in overcoming performance limitations. Beyond material design optimizations (discussed in the prior section), the detector configuration engineering including lateral/vertical heterostructures and phototransistor-enhanced signal amplification has emerged as a crucial approach to enhance key metrics such as g_{Iph}, responsivity and detectivity. Furthermore, synergistic integration with artificial chiral structures and hybridization with other chiral materials (e.g., cholesteric liquid crystals) amplify the differential response of CP light through asymmetric enhancement and polarization-selective reflection, respectively. This section systematically investigates cutting-edge device design strategies and their interplay with chirality-dependent effects to establish multifaceted solutions for the construction of high-performance CP photodetectors and accelerate their practical application process.

5.1. Device Engineering Based on Chiral Metal Halides

This section systematically examines device architectures that exploit the intrinsic chiroptical properties of chiral metal halides for direct CP light detection. Lateral devices benefit from straightforward fabrication and crystallographic orientation control, whereas vertical structures leverage built-in electric fields to improve carrier separation. Phototransistors further offer gate-tunable signal amplification capabilities. Critical challenges remain in balancing chiral effect with overall device performance, ensuring interfacial and environmental stability, and scaling up production—each representing a key frontier for future device optimization.

5.1.1. Lateral Architectures

Lateral-configuration CP photodetectors typically comprise photoconductors and phototransistors (Section 5.1.3), with horizontally aligned electrodes capturing in-plane asymmetric carrier transport. This design is renowned for low fabrication complexity and high crystallographic orientation tunability, particularly suited for probing intrinsic chiral CP-response mechanisms. Early demonstrations using chiral (R-/S-α-PEA)PbI_3 CHMH film-based photoconductors validated the feasibility of this configuration, achieving a g_{res} of ≈0.1 and great ambient stability, with the unencapsulated devices showing almost no degradation after one month at room temperature.[20] Due to the relatively long channel length and low charge carrier concentration in photoconductors, they exhibit higher resistance. Therefore, employing chiral metal halides with high carrier mobility and long carrier lifetime is essential for enhancing the performance of CP photoconductor, since such materials enable efficient collection of carriers associated with photoconductive gain. It should be noted that high anisotropic factors in these systems typically rely on low-dimensional systems. For instance, devices based on chiral 2D [(R/S)-3APr]PbI_4 single-crystal films with DJ-phase structure which can reduce exciton binding energy, achieve a high g_{Iph} of 0.65 and a detectivity of 5.3×10^{13} Jones.[24] In addition, these systems can offer distinctive photophysical properties. The chiral 2D $(R\text{-}BPEA)_2PbI_4$ (R-BPEA = (R)-1-(4-bromophenyl)ethylammonium) exhibit a strong two-photon absorption coefficient of 55 cm/MW due to strong light-matter interactions in quantum well structures, enabling visible-to-NIR dual-mode CP light detection, providing a promising route to improve CP light detector sensitivity and night vision capabilities.[25]

However, the lateral photodetectors commonly face a fundamental trade-off between high chiroptical response and

overall device performance. The quasi-2D (R/S-NEA)$_2$(MA)$_2$Pb$_3$I$_{10}$ films achieves a high photoresponsivity of 15.7 A W^{-1}, while its g_{res} remains only 0.15.[123] 3D systems may provide alternative pathways toward performance balance. The chiral 3D (S-BPEA)EA$_6$Pb$_4$Cl$_{15}$ incorporates large chiral cations within the "hollow" inorganic framework formed via mixed-cation interactions, its single-crystal device demonstrates balanced performance across a linear dynamic range (73.26 dB), responsivity (1.87 mA W^{-1}), detectivity (4.70 × 10^{10} Jones), and g_{Iph} (0.28).[26] Specifically, by constructing periodic micro/nanowire arrays on the photodetector surface to enable directed chiral carrier separation and defect-free transport channels, the CP light detection performance can be significantly enhanced, achieving high responsivity of tens of A W^{-1} and high detectivity on the order of 10^{13}.[49,177] It is worth emphasizing that the one-step capillary bridge assembly technique enables the wafer-scale integration of aligned, uniformly sized chiral lead halide microwire arrays.[49] This array CP photodetector exhibits excellent optoelectronic performance, with a high responsivity of 86.7 A W^{-1}, an unprecedented detectivity exceeding 4.84 × 10^{13} Jones, a high anisotropy factor of 0.42, and high-fidelity CP imaging with 256 pixels. Nevertheless, uniformity in large-scale fabrication remains a critical obstacle to practical application, particularly in micro/nanowire array configurations, where minor deviations in wire size or orientation can lead to inconsistent polarization responses.

The construction of heterostructures allows for the integration of exceptional chiroptical absorption and efficient carrier transport properties from different materials. Furthermore, the built-in electric field at the heterojunction enhances the separation efficiency of photogenerated carriers, leading to an increased spin-polarized current and a higher photocurrent anisotropy factor. The CP photodetector based on chiral 2D (R-MBA)$_2$PbI$_4$ and 2D MoS$_2$ heterostructures exhibits exceptional detection performance with a high responsivity of 0.45 A/W, which is almost 2 orders of magnitude higher than that of CP photodetectors based on metamaterials, and a detectivity of 2.2 × 10^{11} Jones, comparable to that of 3D perovskite/MoS$_2$ photodetectors.[48] The heterostructure crystal (R-MPA)$_2$MAPb$_2$I$_7$/MAPbI$_3$ integrates a chiral 2D lead halide single crystal with its 3D counterpart through a solution-processed heteroepitaxial strategy. This heterostructure features a near-atomic-level sharp interface, which facilitates the formation of a built-in electric field that suppresses photogenerated carrier recombination while preserving chiroptical activity. The resulting photodetector (**Figure** 8a-i) demonstrates significantly amplified CP photodetection sensitivity at 0 V with an impressive g_{res} up to 0.67, which is about six times higher than that of the single-phase 2D chiral lead halide CP photodetector and exceeds many other CP photodetectors based on chiral semiconductors, while also maintaining good stability with no significant photoresponse loss after 30 days in air.[30] Despite such demonstrations of stability over 30 days, environmental stability remains a critical yet underreported constraint, and far more research is needed to ensure long-term operational reliability for practical applications.

The straightforward architecture of lateral configurations facilitates the development of flexible CPL detectors, paving the way for their application in wearable electronics. Integrating chiral perovskite films on flexible substrates such as polyethylene terephthalate (PET) enables mechanical compliance while retaining chiroptical functionality. For example, uniaxially aligned (R-β-MPA)$_2$MAPb$_2$I$_7$ films with homogeneous energy landscapes achieve a responsivity of 1.1 A W^{-1}, a detectivity of 2.3 × 10^{11} Jones, and a g_{Iph} of 0.2 at 10 V bias while retaining > 90% initial performance after 100 bending cycles (Figure 8a-ii).[22] Further advances include surfactant-mediated uniaxial (R/S-NEA)PbI$_3$ (NEA = 1-(1naphthyl)ethylamine) films, which yield a specific detectivity of 5.23 × 10^{13} Jones—tenfold higher than non-oriented counterparts—and a photocurrent anisotropy factor of 0.7, enabling filter-free full-Stokes polarimetry alongside excellent mechanical durability.[21]

5.1.2. Vertical Architectures

Vertical two-terminal architectures primarily comprise photodiodes, whose core advantage lies in their ability to leverage the intrinsic high electric field and optimized depletion region to significantly enhance electron-hole pair separation efficiency under illumination.[4] Such devices commonly employ transparent indium tin oxide (ITO) as the electrode to facilitate light signal reception.[27,32,130,139,202] Although the EQE of typical photodiodes is limited to 100% and typically falls below that of photoconductors and phototransistors due to inevitable charge recombination, their performance can be optimized through meticulous design of the energy level alignment and compatibility among light-harvesting layers, transport layers, and electrodes. For instance, a multilayer architecture of Au/spiro-OMeTAD/urea-doped chiral perovskite/ZnS-modified mesoporous TiO$_2$ (mp-TiO$_2$)/ITO (Figure 8b) achieves enhanced performance.[130] In this design, the ZnS-modified mp-TiO$_2$ electron transport layer optimizes band alignment with the perovskite absorber and suppresses interfacial charge recombination, while urea doping in the CHMH layer improves crystallinity and charge extraction efficiency. Consequently, both photoresponsivity (0.43 A W^{-1}) and distinguishability (g_{res} = 0.27) are enhanced by factors of 1.26 and 2.60, respectively, compared to non-doped CHMH devices.[27]

Similar to lateral architectures, vertically configured devices also utilize heterostructure engineering to enhance performance. A notable example involves the integration of chiral lead halide single crystals onto silicon substrates, forming a UV-sensitive heterostructure for CP light detection in the sun-blind spectrum.[111] The built-in electric field in this structure promotes efficient carrier separation, yielding an anisotropy factor (0.4) at zero bias that exceeds single-phase chiral lead halides by over 4 times. Concurrently, the ultra-low dark current in self-driven operation mode yields a detectivity (1.2 × 10^{12} Jones) approximately two orders of magnitude greater. Another advancement employs a type I heterojunction between chiral 2D (R-α-PEA)$_2$PbI$_4$ and 3D MAPbI$_3$, fabricated through an intermittent spin-coating process.[129] Compared to pure 2D systems, this 2D/3D heterostructure device exhibits the doubled photocurrent and distinct photocurrent levels under LCP and RCP illumination, effectively demonstrating the role of the 3D phase as a charge transport channel in enhancing carrier collection efficiency and overall detection performance.

A fundamental advantage of photodiodes over lateral architectures is their ability to utilize the built-in electric field for

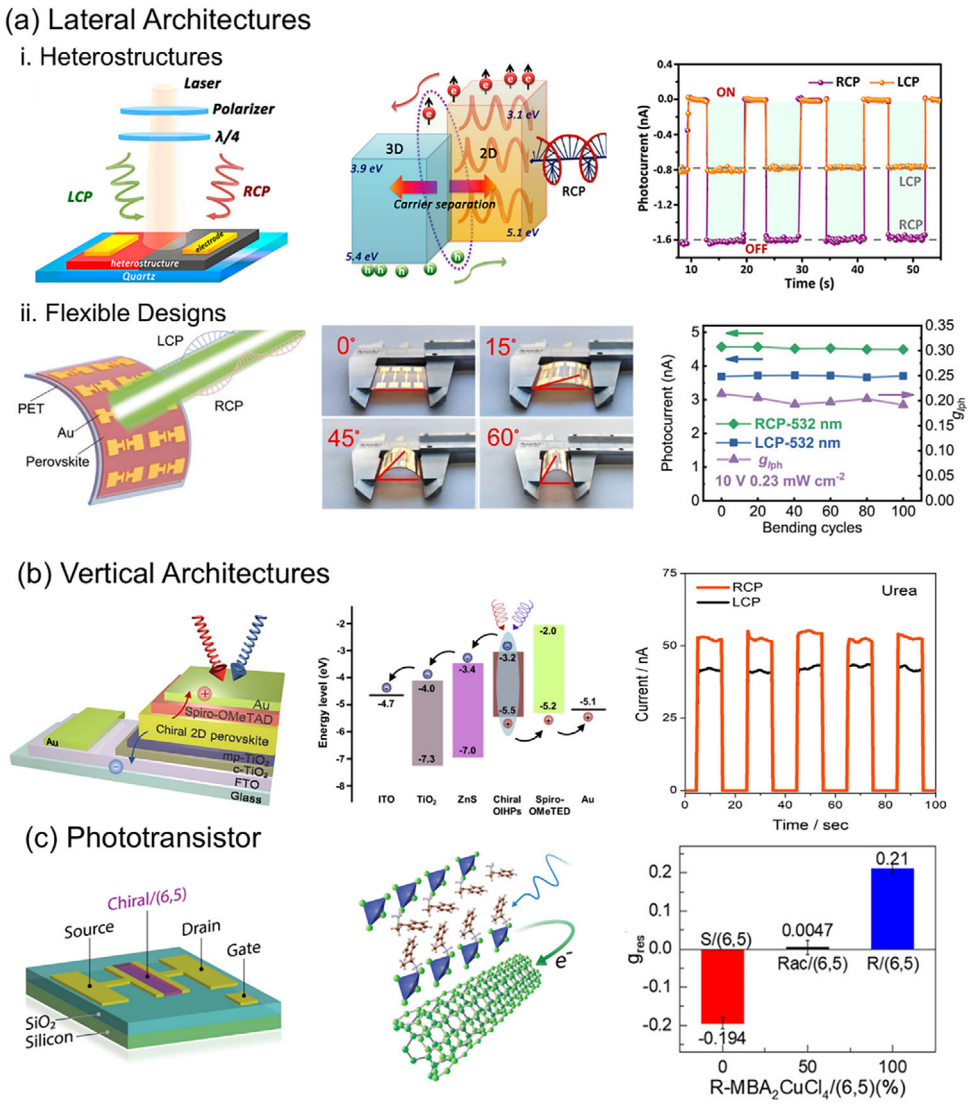

Figure 8. Architectures and performance of chiral metal halide CP photodetectors: a) Lateral-type CP photodetector with CHMHs. Reproduced with permission.[22,30] Copyright 2021, American Chemical Society. Copyright 2020, Wiley-VCH. b) Vertical-type CP photodetectors with CHMHs. Reproduced with permission.[130] Copyright 2022, American Chemical Society. c) Phototransistor based on the (R-/S-MBA)$_2$CuCl$_4$/SWCNT heterostructure. Reproduced with permission.[29] Copyright 2021, American Chemical Society.

photogenerated carrier separation, enabling self-powered photodetection without requiring external electrical bias. This self-powering mechanism not only reduces energy consumption and simplifies system design but also eliminates additional noise introduced by applied bias, making it crucial for portable and low-power applications. Combined with specific molecular engineering of light-harvesting components, devices can achieve excellent CP light response at 0 V bias. A CP photodetector employing 1D CHMHs based on ortho-substituted carbazolylethylamine (oCPEA) ligands through the ITO/PEDOT:PSS/CHMHs/Bathocuproine/Ag architecture, achieves a high g_{Ph} value of 1.25 under a self-powered real-time sensing mode.[139] Similarly, a device constructed with TADDOL-doped (R/S-MBA)$_2$PbI$_4$ films in an ITO/CHMHs/MoO$_3$/Au configuration yields a g_{Ph} exceeding 1.1 under zero-bias operation.[32]

5.1.3. Phototransistor

In contrast to conventional two-terminal photodetectors, phototransistors employ a three-terminal architecture where an applied gate voltage precisely modulates the semiconductors' charge carrier density, enabling signal amplification by over three orders of magnitude.[16] A notable example is the MBA$_2$CuCl$_4$/SWCNT (SWCNT = single-walled carbon nanotube) heterostructure, which achieves record-high photoresponsivity of 452 A/W and a g_{res} of 0.21 through pin-selective charge transfer (Figure 8c).[29] Similarly, chiral R-/S-MBABr-functionalized CsPbBr$_3$ NCs combined with SWCNTs enable clear discrimination of CPL with average g_{ph} of 0.143 ± 0.028 and -0.089 ± 0.020, respectively.[76] Besides, the (S-MBA)$_2$(MA)$_{n-1}$PbnI$_{3n+1}$ thin film field effect transistor exhibits a responsivity of 0.15 A W^{-1} and a detectivity of

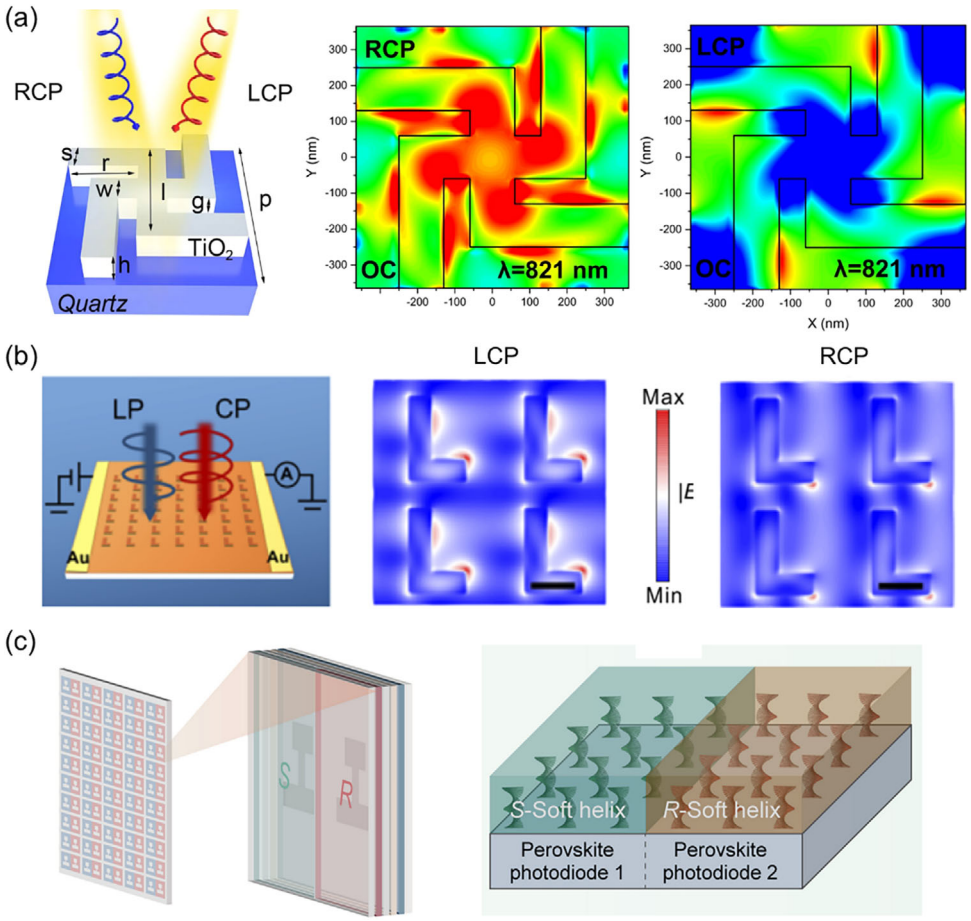

Figure 9. CP light detection strategies based on achiral metal halides: a) Left-handed perovskite chiral metamolecule on quartz substrate. Optical chirality maps at 821 nm reveal distinct LCP/RCP spatial distributions. Reproduced with permission.[204] Copyright 2022, Springer Nature. b) HMH metasurface and its simulated LCP/RCP electric fields at 650 nm (scale bars: 200 nm).[205] c) Soft-helix-layer-decorated perovskite photodiode for CP light detection. Reproduced with permission.[34] Copyright 2022, Optica Publishing Group.

1.4×10^8 Jones under LCP light illumination, while that of $(R\text{-}MBA)_2(MA)_{n\text{-}1}PbnI_{3n+1}$ are 0.14 A W^{-1} and 1.3×10^8 Jones under RCP light illumination.[203] Additionally, the device demonstrates temperature-dependent charge transport characteristics over a wide range of temperatures (80–300 K). This work deepens understanding of the charge transport mechanisms in chiral perovskite materials.

5.2. CP Light Detection Strategies Based on Achiral Metal Halides

Beyond leveraging the intrinsic chirality of chiral metal halides for CP light detection, it is also possible to equip achiral metal halide photodetectors with the ability to discriminate CP light through rational design of artificial chiral structures or hybridization with chiral materials. These extrinsic chirality strategies not only broaden the range of usable materials but also extend the operational wavelength range of the devices. This provides a promising pathway for developing high-performance, low-cost, and easily integrated CPL photodetection platforms.

5.2.1. Enhancement with Artificial Chiral Structures

The top-down chiral metasurface strategy enables precise chirality transfer to metal halide systems through engineered superstructures. Unlike CP photodetectors based on inherently chiral metal halides, which primarily exhibit chiroptical responses in the UV–visible range, these devices typically demonstrate chiroptical responses at longer wavelengths. The chiral superstructure of $MAPbI_3$ metal halides with gammadion metamolecule is shown in **Figure 9**a.[204] Optical chirality (OC) analysis reveals a distinct inversion in OC values under LCP and RCP light illumination at 821 nm within the left-handed chiral metasurface unit cell. The perovskite metasurface with an array area of ≈20 μm × 20 μm obtains a g_{CD} of 0.49, and the simulation results show that the g_{CD} of the device with a larger area can be further improved to 1.11. CP light sensitivity can also be achieved by designing mirrored asymmetric assemblies on top of metal halide films. The L-shaped perovskite nanoantenna array architecture (Figure 9b) enhances responsivity and detectivity by minimizing photoinduced carrier transport distances.[205] At a 5 μm channel length, the device achieves the responsivity of 0.3 A W^{-1} and the detectivity of 3×10^{10} Jones.

5.2.2. Hybridization with Other Chiral Materials

Chiral liquid crystals, as soft helices with 1D photonic crystals, are fascinating materials that can almost perfectly modulate CP light and selectively transmit and reflect CP light of different chirality.[34,206–208] Compared with traditional optical components, the addition of chiral liquid crystals layers to perovskite-liquid crystal photodetectors has the advantages of easy manufacturing, low cost, compact and flexible device design, and reduced propagation loss. The CP photodetector fabricated by combining perovskite single crystals with free-standing cholesteric liquid crystal polymer films exhibits a broadly tunable spectral response through precise modulation of the cholesteric liquid crystal polymer's photonic bandgap. Notably, the detector achieves an impressive g_{Iph} of 1.95, surpassing existing chiral semiconductor-based CP photodetectors and approaching the theoretical limit of 2.0.[208] Recently, the introduction of an innovative paired perovskite-liquid crystal photodetector structure has enabled quantitative detection of diverse circular polarization states (Figure 9c).[34] This design addresses the limitation of traditional CP photodetectors, which struggle to provide effective polarization information from a single beam of unknown polarization state. The device consists of a pair of chiral liquid crystals with opposite chirality and two perovskite photodiodes. By leveraging the selective reflection and transmission properties of the chiral liquid crystals layer alongside the distinct photoelectric responses of the diodes, the circular polarization degree is determined through current difference calculations. The detection results align closely with the Stokes parameter, confirming the reliability and accuracy of the findings.

6. Developing Applications of Chiral Metal Halide CP Photodetectors

Chiral metal halide CP photodetectors leverage tunable chiral photoelectric properties and strong spin-orbit coupling effects to achieve near-theoretical-limit CP light discrimination (g_{Iph} approaching 2), broadband spectral responsivity (UV-visible to NIR), high responsivity and self-powered operation. These capabilities position them as transformative tools for high-precision circular polarization imaging, dynamic information encryption and bionic neuromorphic perception, while holding promise for applications in quantum communication, bridging advanced photonics with emerging applications in quantum technology and adaptive optoelectronics.

6.1. Circular Polarization Imaging

Chiral metal halides CP photodetectors enable high-fidelity circular polarization imaging through their intrinsic circular polarization-sensitive photoresponse. A typical circular polarization imaging system consists of a light source, a linear polarizer (POL), a quarter-wave plate (QWP), and a photoelectronic imaging unit with a patterned photomask. Under LCP and RCP light illumination, the system captures images with significant intensity contrast, yielding well-defined geometric patterns such as the five-pointed star[177] and the 'NKU' lettering.[21] This typically requires the device to exhibit strong discrimination capability, fast response speed, high sensitivity, and a large photocurrent/dark current ratio under CP light excitation. Chiral 2D lead halide-based CP photodetector with a high g_{Iph} of up to 0.72 enable information encryption by deciphering rapid-response (QR) code patterns under CP light illumination (**Figure 10a**).[209] It is noteworthy that such encryption strategies incorporate circular polarization imaging functionality, reflecting the multifunctional capabilities demonstrated by various types of CP photodetectors. Thus, the representative work presented here serves only as an example within this application domain and should not be construed as limiting the device to a single functionality.

Circular polarization imaging has been demonstrated not only at the single-device level but also extended to small-scale arrays and even wafer-scale integration. For instance, a wafer-integrated (R/S-PyEA)Pb_2Br_6 array devices on Si/SiO_2 substrates achieves a 16 × 16 pixel cross-shaped pattern (Figure 10b).[49] The fabrication method emphasizes compatibility with semiconductor manufacturing processes, offering a viable route for the large-scale integration of high-performance chiroptical devices. Moreover, the mechanical stability of flexible devices under bending stress ensures reliable performance on non-planar substrates, highlighting their potential for deformable and wearable CP light imaging platforms.[21,34]

SHG-CD exhibits enhanced sensitivity to chiral structures compared to conventional CD, enabling high-resolution spatial mapping of chiroptical activity.[210–212] In SHG-CD microarea imaging of CHMH films, spatially resolved maps (10 μm × 10 μm) of CHMH under LCP and RCP light excitation exhibit distinct position-dependent SHG intensity patterns (Figure 10c).[210] This spatially correlated chirality arises from localized out-of-plane supramolecular orientation, enabling direct visualization of microstructural asymmetry. Such capability establishes SHG-CD as a precision tool for detecting microscopic chiral features, with applications spanning high-contrast biological tissue imaging[213,214] and non-destructive material ultrastructure analysis.

6.2. Information Encryption

Chiral metal halides, due to their unique CD and SHG-CD effects that are difficult to counterfeit, offer a robust solution for advanced information encryption. For instance, Chiroptical synaptic memristors (CSMs) based on 2D CHMHs consolidate the functionalities of data storage, encryption, and optoneuromorphic operation.[215] By combining CP sensitivity with photoresponsive electrical behavior, these devices exhibit reconfigurable physical unclonable function (PUF) capabilities.

As shown in **Figure 11a**, a 10 × 10 CSM crossbar array demonstrates programmable PUF operation, where reconfigurable cryptographic keys are regenerated through the combination of neuromorphic potentiation and polarized light conditions. This adaptive PUF architecture addresses security challenges in emerging applications such as secure IoT devices, financial transactions, and defense systems, where real-time reconfigurability and hardware-level authentication are paramount. Furthermore, by combining CP light inputs (LCP/RCP) with voltage modulation, the SHG signal intensity of chiral ferroelectric 2D HMHs can execute exclusive OR (XOR) logic

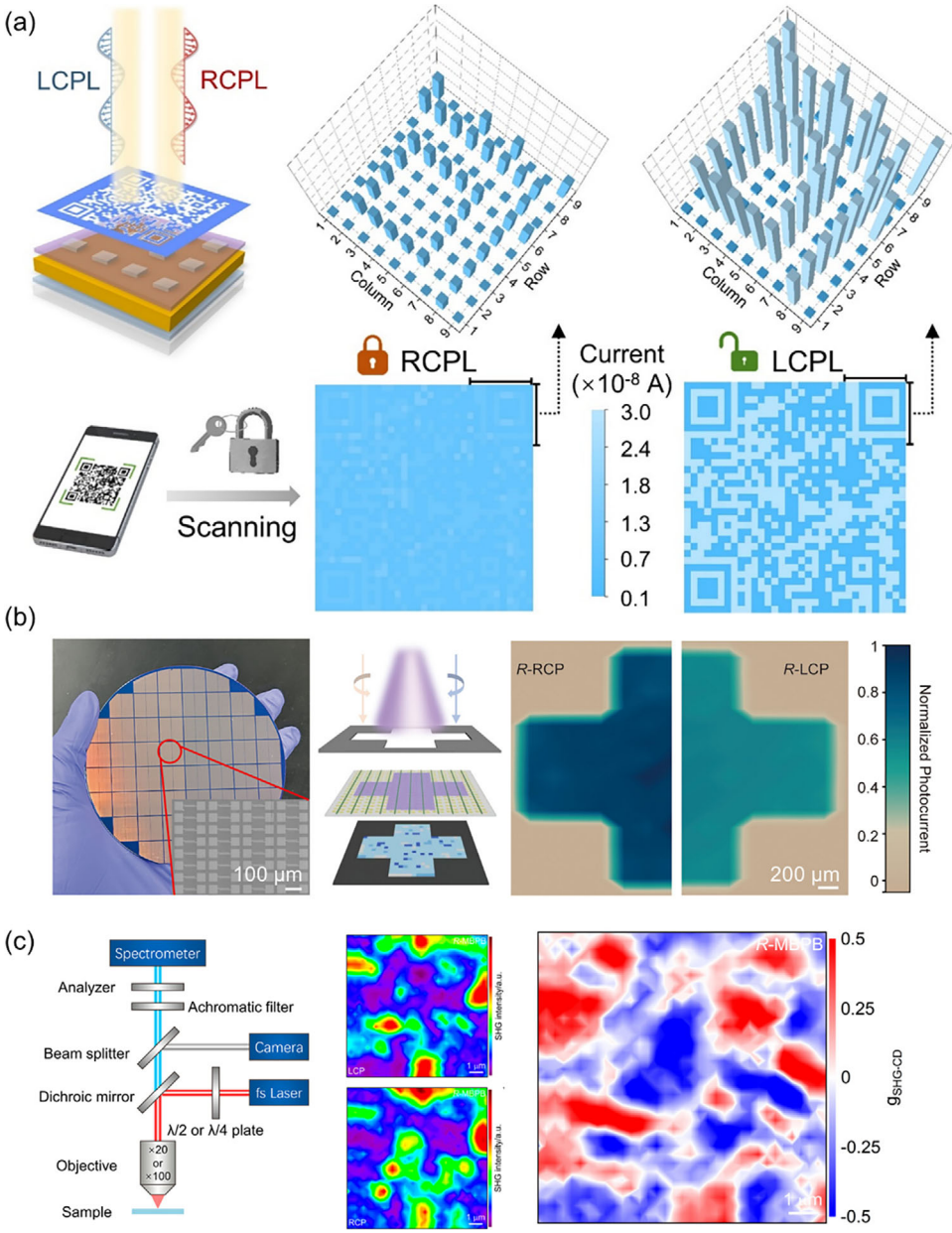

Figure 10. a) Proof-of-concept encrypted QR code imaging of the chiral 2D lead halide-based CP photodetector. Reproduced with permission.[209] Copyright 2025, Wiley-VCH. b) Digital photo of microwire arrays fabrication on a 4 in. silicon dioxide wafer. Inset: Magnified microwire arrays. A schematic illustration of the imaging sensing system. Imaging results of the cross-shaped pattern for the perovskite array device under RCP and LCP illumination. Reproduced with permission.[49] Copyright 2024, American Chemical Society. c) Spatially analyzed SHG images of CHMH under LCP and RCP stimulation; $g_{SHG\text{-}CD}$ image computed in a pixelwise manner from SHG images. Reproduced with permission.[210] Copyright 2023, American Chemical Society.

operations (Figure 11b,c).[216] In the experimental demonstration, the ASCII-encoded message "LOVE" is converted into a cryptic SHG signal sequence, which can only be decrypted and restored by the authorized receiver possessing the decryption key, thereby effectively preventing eavesdropping (Figure 11d). This optical-electrical coordinated modulation mechanism offers a single-component integrated solution for next-generation secure optical communication systems, with anti-interference and anti-modeling attack capabilities.

6.3. Neuromorphic Perception

CP photodetection technology based on chiral metal halides emerges as a transformative approach in bionic vision and neuromorphic computing.[4,51,217] Leveraging the intrinsic chiroptical properties and spin-polarized carrier transport mechanisms of these materials, this technology enables multidimensional breakthroughs spanning from fundamental light perception to the advanced in-memory logic operations. Chiral metal halides allow

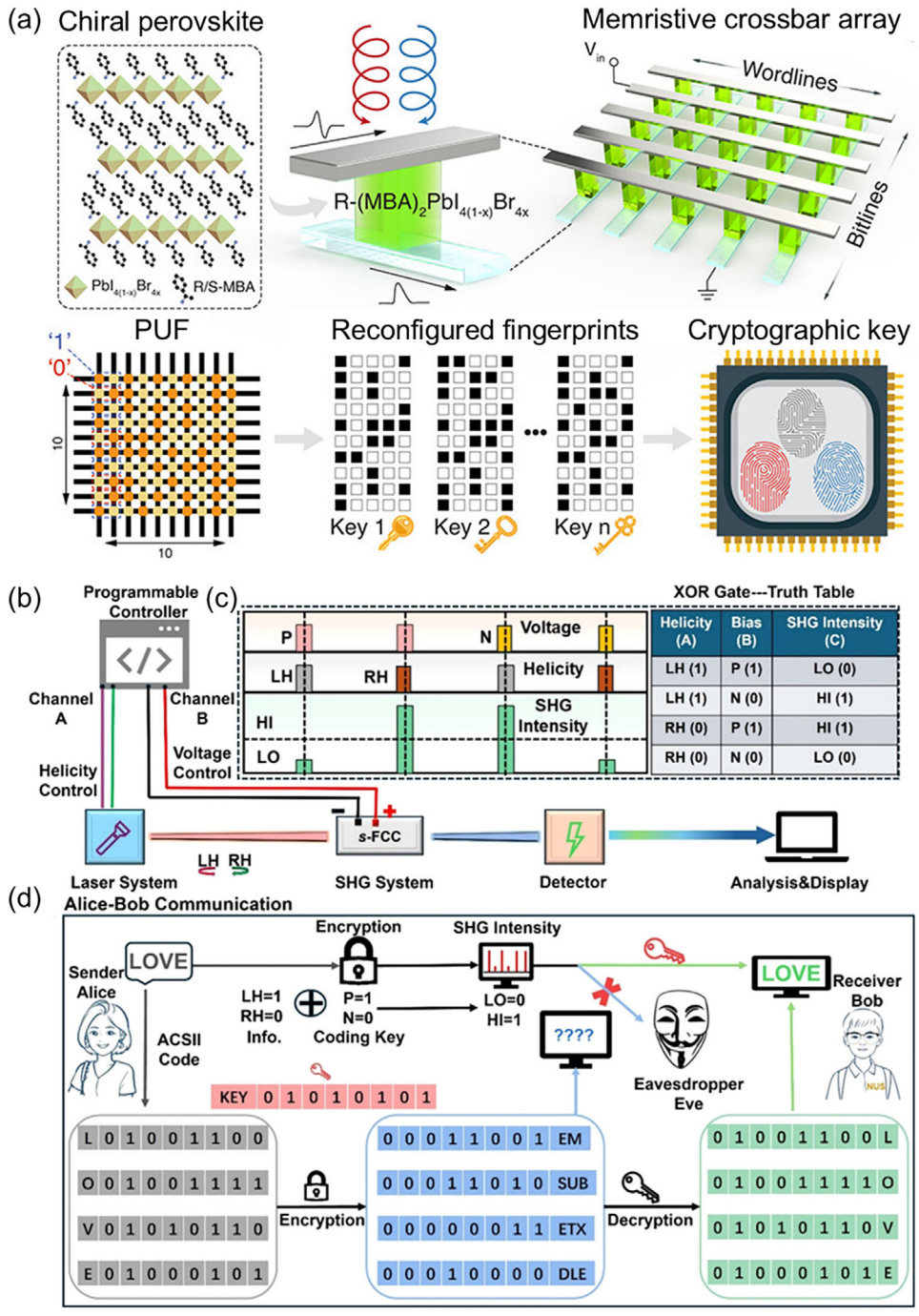

Figure 11. a) A 10 × 10 CSM crossbar array for programmable PUF operation. Reproduced with permission.[215] Copyright 2024, American Chemical Society. b) Schematic of the encrypted optical communication system, including a programmable controller to edit laser (LH and RH) and voltage (positive and negative) sequences, a laser source system, an electrode-patterned s-FCC crystal, and a detector (photomultiplier tube). c) SHG signal intensity modulated by the applied voltage and helicity of the excited laser. d) Schematic of the system implemented the well-known Alice-Bob communication in cryptography. Reproduced with permission.[216] Copyright 2024, American Chemical Society.

precise discrimination between LCP and RCP light, and even full-Stokes parameter resolution (including linear/elliptical polarization states). This capability addresses the inherent limitation of human vision in polarization sensing while mimicking biological systems such as the polarization-sensitive vision of mantis shrimps.

For instance, the device designed via a heterostructure integrating CHMH with SWCNTs demonstrates photoresponsivity up to 240 mA W^{-1} at 395 nm and emulates biological synaptic behaviors, including short-term plasticity and long-term plasticity.[51] Furthermore, it achieves visualization, discrimination, and memorization of circularly polarized images with up to

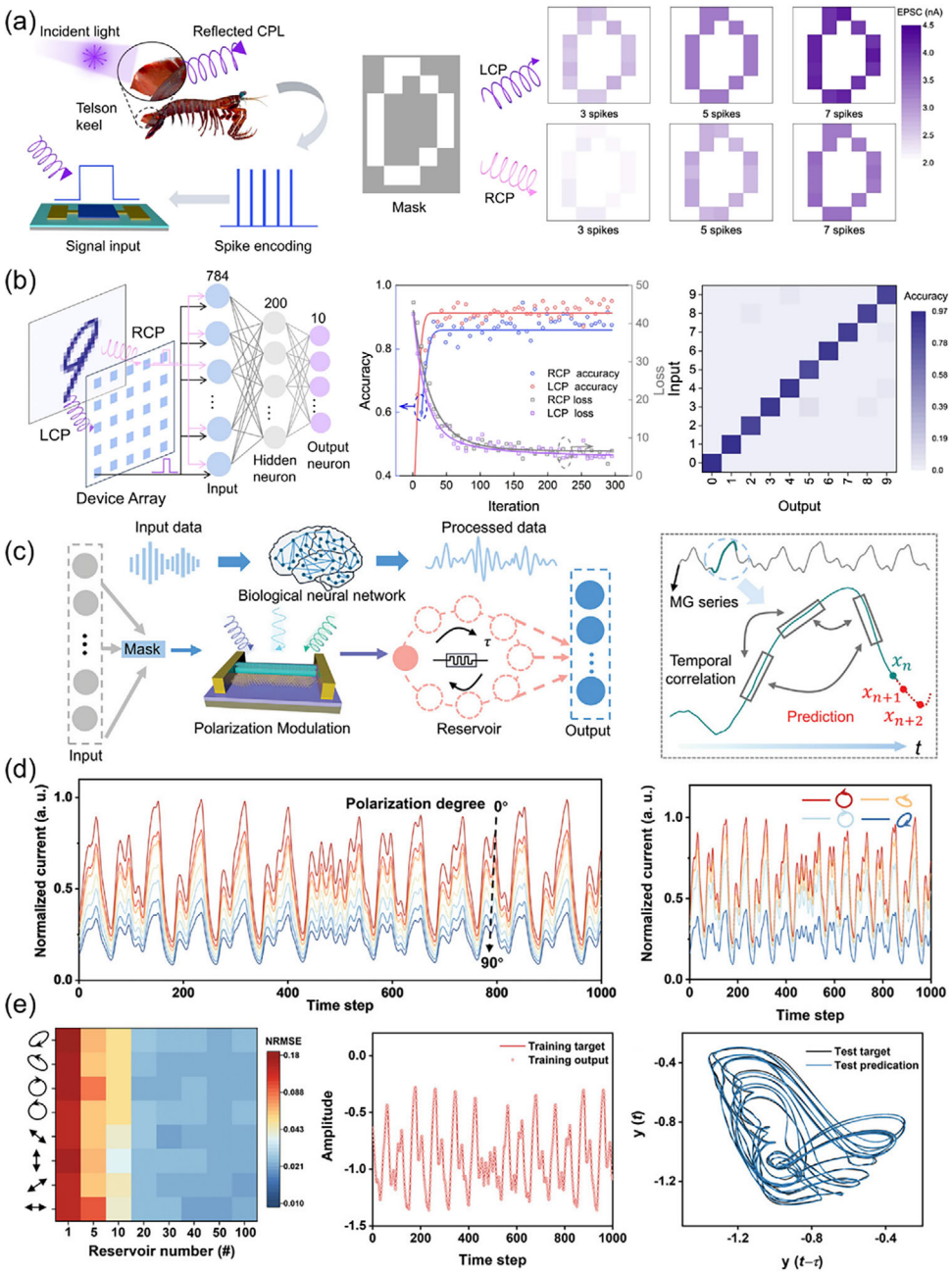

Figure 12. a) The CP light image vision process and CP light-induced memorized graphic. b) Schematic structure, test results and recognition results of PAS device-based neural network. Reproduced with permission.[51] Copyright 2023, Springer Nature. c) Sketch of the RC system in which the PAS serves as the physical reservoir, and MG data processing. d) Dynamic responses of the reservoir and elliptical polarization-enriched reservoir states. e) Analysis of PAS-based RC system performance: Prediction errors across reservoir and states of polarization numbers, training results (target vs. experimental output), and output results in phase space. Reproduced with permission.[180] Copyright 2024, Wiley-VCH.

93% recognition accuracy in spiking neural network simulations (**Figure** 12a,b). These advancements underscore its potential in developing intelligent neuromorphic vision systems.

The structural design of CHMHs has been advanced from thin-film configurations to nanowire architectures. The 1D morphology endows these nanowires with intrinsic linear dichroism and circular dichroism, enabling precise full-Stokes parameter resolution for comprehensive polarization characterization. A single-nanowire-based device demonstrates exceptional performance, achieving a photoresponsivity of 2.3 A W^{-1} while maintaining low power consumption of 0.5 pJ per synaptic stimulus, which is comparable to biological synapse levels.[180] Integration with MXene hole transport layers extends carrier lifetimes to 68 ps through efficient charge extraction, significantly enhancing photoexcited carrier storage. Building upon these innovations, the photonic artificial synapse (PAS)-based reservoir

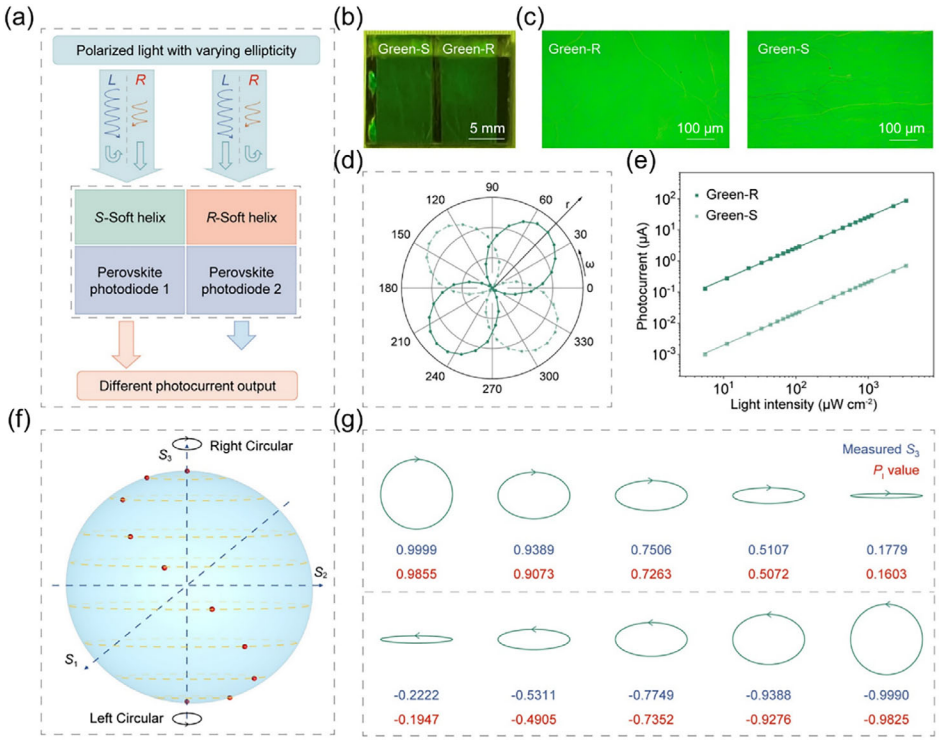

Figure 13. PeLC-PD array device for quantitative detection of polarization states. a) Mechanism and working principle. b) Photograph of a paired green-light-responsive PeLC-PD. c) Polarized optical microscopy (POM) images of R- and S- CLCs in reflection mode. d) Photocurrent recorded under a green laser beam and plotted in a polar coordinate system. ω: polarizer angle; r: photocurrent intensity. Solid and dashed lines correspond to R-CLC (right) and S-CLC (left) devices, respectively. e) Photocurrent response under LCP and RCP light at 0 V. f) Poincaré sphere representation for the polarization states. g) Comparison of polarization-dependent S_3 (ellipticity) extracted from Poincaré sphere representation and devices-measured P_l values. Reproduced with permission.[34] Copyright 2024, Elsevier.

computing (RC) system exhibits remarkable spatiotemporal dynamics, achieving a normalized root mean square error of 0.023 in the Mackey-Glass (MG) time series forecasting task (Figure 12c–e). This breakthrough highlights the system's potential for multimodal perception and parallel processing of complex temporal signals. The spin polarization characteristics of chiral materials enable in-memory logic operations. Devices based on R- and S-configuration CHMHs exhibit markedly distinct excitatory postsynaptic currents under CP light illumination, demonstrating spin polarization efficiencies exceeding 83% through chirality-induced spin selectivity.[218] Strategic alignment between material chirality and CP light handedness activates complementary logic functions: while an R-device functioned as an AND gate, the device based on the same HMH of an S-device acted as a NOR gate for in-memory logic operations. This CP light-driven logic paradigm eliminates auxiliary circuitry requirements, establishing a new hardware framework for multidimensional optical information processing and brain-inspired computing architectures.

6.4. Quantum Communication

Chiral metal halides show significant potential for use in quantum communication systems due to their high polarization discrimination efficiency and spin-selective photoresponse. These materials can serve as on-chip circular polarization filters and single-photon detectors, which are critical for quantum key distribution and spin-photon interfaces.[219,220] Their compatibility with silicon photonics and flexible substrates suggests a viable route toward integrated quantum photonic circuits. Although still an emerging field, recent demonstrations of metal halide-based photodetectors have overcome the limitations of incomplete polarization parameter extraction typical of conventional CP photodetectors. As shown in **Figure 13**, paired perovskite-liquid crystal photodetectors (PeLC-PD) were constructed to quantify the ellipticity of arbitrary polarized light.[34] The device consists of a pair of opposite-handed chiral liquid crystals (CLCs) and two perovskite photodiodes. By leveraging the selective reflection and transmission of polarized light by the CLC layers, combined with the differential photoresponses of the two diodes, the circular polarization degree (P_l) is quantitatively determined based on the current contrast. The detection results demonstrate strong consistency with Stokes parameter S_3. The high solution processability of perovskites and cholesteric liquid crystals not only simplifies integration with existing systems but also enhances sensitivity and responsivity by reducing light interaction path lengths. This advance underscores the potential of chiral metal halides for secure quantum communication applications, offering a promising pathway toward integrable and highly precise CP photodetection for quantum information processing and cryptography.

Table 3. Summary of characteristics of chiral metal halide CP photodetectors.

Materials	Highest $\|g_{abs}\|$	Highest $\|g_{Iph}\|/\|g_{res}\|$	Responsivity [A W^{-1}]	Detectivity [Jones]	Refs.
(R/S-α-PEA)PbI_3	0.02	0.1	0.797	7.1×10^{11}	[20]
(R/S-3APr)PbI_4	0.00117	0.65	1.06	\	[24]
(R-BPEA)$_2PbI_4$	0.003	0.1	0.0021	3×10^{11}	[25]
(S-BPEA)$EA_6Pb_4Cl_{15}$	0.000076	0.28	0.00187	4.7×10^{10}	[26]
(R-3AMP)$PbBr_4$	0.0018	0.2	0.00419	2.4×10^{12}	[28]
(R-NEA)PbI_3	0.04	1.85	0.28	\	[33]
(R-β-MPA)$_2MAPb_2I_7$	\	0.2	1.1	2.3×10^{11}	[22]
(R-β-MPA)$_4AgBiI_8$	\	0.3	2.2×10^{-5}	1.2×10^{7}	[127]
(R-β-MPA)$EA_2Pb_2Br_7$	0.00046	0.03	8.1×10^{-5}	1.2×10^{9}	[23]
(R/S-MBA)$_2Pb_{0.9}Sn_{0.1}I_4$	0.0016	0.44	0.14	1.63×10^{11}	[27]
(S-MBA)PbI_3	0.00286	0.31	0.83	3.63×10^{12}	[117]
(R-NEA)PbI_3	\	0.294	0.09	3.8×10^{11}	[110]
(S-MBA)$_2Pb(I_{0.7}Br_{0.3})_4$	0.001	0.27	0.43	6.02×10^{12}	[130]
(R/S-NEA)$_2(MA)_{n-1}Pb_nI_{3n+1}$	0.005	0.15	15.7	\	[123]
(R-MBA)$_2PbI_4$	\	0.23	0.6	3.06×10^{11}	[128]
(R-3AMP)$PbBr_4$	0.0018	0.22	0.0419	2.4×10^{12}	[28]
(R-β-MPA)$EAPbBr_4$	0.002	0.16	\	1.1×10^{11}	[96]
(R/S-MBA)$_2PbI_4$	0.0055	0.1	\	\	[74]
(R-PPA)$EAPbCl_4$	0.0033	0.4	\	4.5×10^{7}	[98]
(R-MBA$_{0.5}n$BA$_{0.5}$)$_2PbI_4$	0.00289	0.58	0.142	2.45×10^{12}	[146]
(R/S-PPA)$PAPbBr_4$	0.0048	0.5	\	\	[142]
(R-PPA)$EAPbBr_4$	0.0025	0.42	\	\	[147]
(S-MBA)$_2PbI_4$	0.00054	0.209	0.433	4.62×10^{10}	[137]
(S-2F-MBA)$_2PbI_4$	0.00168	0.288	0.591	5.68×10^{10}	[137]
(S-4F-MBA)$_2PbI_4$	0.000309	0.13	0.578	5.56×10^{10}	[137]
(R-/S-α-PEA)$_2PbI_4$	\	0.15	41.3	1.24×10^{13}	[177]
$MAPbBr_3$	0.004	0.39	1.48×10^{-4}	\	[52]
(R-NEA)PbI_3	0.042	0.7	0.96	5.23×10^{13}	[21]
(R-MBA)$CuCl_4$/SWCNT	0.1	0.25	452	\	[29]
(R-MPA)$_2MAPb_2I_7/MAPbI_3$	\	0.67	0.0012	1.1×10^{12}	[30]
(R-BPEA)$_2PbI_4/MAPbI_3$	\	0.25	\	8.2×10^{10}	[112]
(R/S-β-MPA)$_2PbI_4$/(R/S-β-MPA)$_2MA_{n-1}Pb_nI_{3n+1}$	\	0.38	22.14	\	[31]
TADDOL-doped (S-MBA)$_2PbI_4$	0.00579	1.16	0.17	3.63×10^{12}	[32]
Lead halide-liquid crystals	1.7	1.96	0.294	\	[34]

7. Summary and Perspectives

The exceptional performance of chiral metal halide CP photodetectors stems from the coordinated optimization of material design and their unique physical mechanisms. With strong SOC and intrinsic chirality, CHMHs achieve efficient resolution of CP light through CD and CISS effects. The asymmetric photocurrent response depends not only on the generation of spin-polarized carriers but also on the spin-dependent charge transport and collection.[19] Specifically, under LCP or RCP light illumination, angular momentum transfer generates carriers with specific spin states according to optical selection rules, while the CISS effect exerts selective transport resistance on carriers with specific spins through the chirality of CHMHs, thus amplifying the asymmetric photocurrent response ($g_{Iph} \gg g_{abs}$).[72,130,139,221] The device architecture has progressed from simple conventional designs to advanced systems incorporating artificial chiral structures or liquid crystals, yielding significant performance enhancements (**Table 3**). These developments have led to key breakthroughs including a giant g_{Iph} (>1.9), wafer-level integrated polarization detection capabilities, and applications in cutting-edge fields like encryption and intelligent perception systems. Addressing challenges in the following three areas is crucial for further advances:

1) Developing stable chiral material systems that exhibit strong chiroptical activity and efficient photoelectric transport remains a fundamental challenge. Research efforts should prioritize replacing lead-based systems with non-toxic, stable alternatives (e.g., Sn-, Bi-, or Cu-based compounds)

and constructing 3D chiral architectures to enhance spin-related properties. Integrating machine learning with high-throughput screening could accelerate the discovery of novel chiral ligands and hybrid structures, while employing hierarchical chirality strategies (combining molecular chirality with supramolecular or lattice-level asymmetry) could amplify anisotropy factors without compromising optoelectronic efficiency.

2) Deepening the mechanistic understanding and developing innovative characterization methods is essential to guide material and device design. A primary obstacle is the incomplete knowledge of how atomic/molecular-scale chirality translates to macroscopic spin-polarized phenomena, such as the role of chiral distortions in modulating Rashba-Dresselhaus splitting or spin-dependent carrier recombination. Bridging this gap requires collaboration between advanced theoretical modeling and innovative experimental techniques. Spin-resolved DFT and quantum transport simulations should be coupled with operando characterization methods—such as time-resolved CD spectroscopy and spin-polarized scanning tunneling microscopy—to directly probe the structural evolution and spin polarization processes under operating conditions. Furthermore, developing novel in situ chiroptical techniques and establishing standardized metrics (e.g., chirality-to-spin conversion efficiency) will be pivotal for quantitatively comparing material systems and accelerating the development of high-performance chiral optoelectronic devices.
3) Advancing system integration and interdisciplinary convergence is crucial for emerging applications. Efficient large-area manufacturing techniques—such as roll-to-roll processing or inkjet printing—for high-quality chiral metal halide films are essential to advance from single-device demonstrations to functional photodetector arrays, particularly through back-end-of-line integration with CMOS or monolithic silicon-photonics wafers. This progress will enable applications beyond conventional optics, including those in quantum sensing and quantum information processing that leverage the spin selectivity and room-temperature spin polarization of CHMHs. Furthermore, integrating CHMHs with spin photonic devices could lead to novel spin-based light sources and detectors. This synergy paves the way for chip-scale spin-photonic circuits and accelerates the development of quantum-classical hybrid systems for integrating quantum internet with existing communication infrastructure.

Acknowledgements

This work was supported by National Natural Science Foundation of China (Nos. 52425308, 62204047, 62374035 and 92263106).

Conflict of Interest

The authors declare no conflict of interest.

Keywords

chirality, circular polarized light detection, metal halides, photodetectors

Received: April 27, 2025
Revised: September 7, 2025
Published online:

[1] X. Wang, Y. Wang, W. Gao, L. Song, C. Ran, Y. Chen, W. Huang, *Adv. Mater.* **2021**, *33*, 2003615.
[2] Z. A. VanOrman, W. R. Kitzmann, A.-P. M. Reponen, T. Deshpande, H. J. Jöbsis, S. Feldmann, *Nat. Rev. Chem.* **2025**, *9*, 208.
[3] J. Crassous, M. J. Fuchter, D. E. Freedman, N. A. Kotov, J. Moon, M. C. Beard, S. Feldmann, *Nat. Rev. Mater.* **2023**, *8*, 365.
[4] R. Lu, Y. Li, H. Song, J. Jiang, *Adv. Funct. Mater.* **2025**, *35*, 2423770.
[5] Z. Long, Y. Zhou, Y. Ding, X. Qiu, S. Poddar, Z. Fan, *Nat. Rev. Mater.* **2025**, *10*, 128.
[6] M. Zhang, X. Wu, Z. Wang, L. Sun, Y. Ren, Y. Liu, R. Li, R. Ding, Y. Wei, F. Yang, J. Feng, W. Hu, *Adv. Funct. Mater.* **2025**, *35*, 2423932.
[7] Y. Yang, R. C. da Costa, M. J. Fuchter, A. J. Campbell, *Nat. Photonics* **2013**, *7*, 634.
[8] Y. Kwon, J. Y. Jung, W. B. Lee, J. H. Oh, *Adv. Sci.* **2024**, *11*, 2308262.
[9] J. Ahn, S. H. Lee, I. Song, P. Chidchob, Y. Kwon, J. H. Oh, *Device* **2023**, *1*, 100176.
[10] D. Zhu, W. Jiang, Z. Ma, J. Feng, X. Zhan, C. Lu, J. Liu, J. Liu, Y. Hu, D. Wang, Y. S. Zhao, J. Wang, Z. Wang, L. Jiang, *Nat. Commun.* **2022**, *13*, 3454.
[11] M. Schulz, F. Balzer, D. Scheunemann, O. Arteaga, A. Lützen, S. C. J. Meskers, M. Schiek, *Adv. Funct. Mater.* **2019**, *29*, 1900684.
[12] L. Liu, Y. Yang, Y. Wang, M. A. Adil, Y. Zhao, J. Zhang, K. Chen, D. Deng, H. Zhang, K. Amin, Y. Wu, Y. Zhang, Z. Wei, *ACS Mater. Lett.* **2022**, *4*, 401.
[13] Q. Gu, J. Zha, C. Chen, X. Wang, W. Yao, J. Liu, F. Kang, J. Yang, Y. Y. Li, D. Lei, Z. Tang, Y. Han, C. Tan, Q. Zhang, *Adv. Mater.* **2024**, *36*, 2306414.
[14] X. Tang, J. Zha, X. Wu, J. Tong, Q. Gu, K. Zhang, Y. Zhang, S. Zheng, J. Fan, W. Zhang, Q. Zhang, C. Tan, S. Cai, *Angew. Chem., Int. Ed.* **2025**, *64*, 202413675.
[15] L. Wan, R. Zhang, E. Cho, H. Li, V. Coropceanu, J.-L. Brédas, F. Gao, *Nat. Photonics* **2023**, *17*, 649.
[16] S. D. Namgung, R. M. Kim, Y.-C. Lim, J. W. Lee, N. H. Cho, H. Kim, J.-S. Huh, H. Rhee, S. Nah, M.-K. Song, J.-Y. Kwon, K. T. Nam, *Nat. Commun.* **2022**, *13*, 5081.
[17] W. Li, Z. J. Coppens, L. V. Besteiro, W. Wang, A. O. Govorov, J. Valentine, *Nat. Commun.* **2015**, *6*, 8379.
[18] C. Chen, Z. Yang, T. Hang, Y. Hao, Y. Chen, C. Zhang, J. Yang, X. Liu, X. Li, G. Cao, *Light Sci. Appl.* **2025**, *14*, 265.
[19] G. Long, R. Sabatini, M. I. Saidaminov, G. Lakhwani, A. Rasmita, X. Liu, E. H. Sargent, W. Gao, *Nat. Rev. Mater.* **2020**, *5*, 423.
[20] C. Chen, L. Gao, W. Gao, C. Ge, X. Du, Z. Li, Y. Yang, G. Niu, J. Tang, *Nat. Commun.* **2019**, *10*, 1927.
[21] Q. Chen, Z. Ding, L. Zhang, D. Wang, C. Geng, Y. Feng, J. Zhang, M. Ren, S. Li, S. M. H. Qaid, Y. Jiang, M. Yuan, *Adv. Mater.* **2024**, *36*, 2400493.
[22] L. Wang, Y. Xue, M. Cui, Y. Huang, H. Xu, C. Qin, J. Yang, H. Dai, M. Yuan, *Angew. Chem., Int. Ed.* **2020**, *59*, 6442.
[23] W. Wu, X. Shang, Z. Xu, H. Ye, Y. Yao, X. Chen, M. Hong, J. Luo, L. Li, *Adv. Sci.* **2023**, *10*, 2206070.
[24] L. Wang, W. Hao, B. Peng, J. Ren, H. Li, *Adv. Mater.* **2025**, *37*, 2414199.
[25] Y. Peng, X. Liu, L. Li, Y. Yao, H. Ye, X. Shang, X. Chen, J. Luo, *J. Am. Chem. Soc.* **2021**, *143*, 14077.
[26] Q. Guan, T. Zhu, Z. K. Zhu, H. Ye, S. You, P. Xu, J. Wu, X. Niu, C. Zhang, X. Liu, J. Luo, *Angew. Chem., Int. Ed.* **2023**, *62*, 202307034.
[27] B. Yao, Q. Wei, Y. Yang, W. Zhou, X. Jiang, H. Wang, M. Ma, D. Yu, Y. Yang, Z. Ning, *Nano Lett.* **2023**, *23*, 1938.

[28] C. C. Fan, X. B. Han, B. D. Liang, C. Shi, L. P. Miao, C. Y. Chai, C. D. Liu, Q. Ye, W. Zhang, *Adv. Mater.* **2022**, *34*, 2204119.
[29] J. Hao, H. Lu, L. Mao, X. Chen, M. C. Beard, J. L. Blackburn, *ACS Nano* **2021**, *15*, 7608.
[30] X. Zhang, X. Liu, L. Li, C. Ji, Y. Yao, J. Luo, *ACS Cent. Sci.* **2021**, *7*, 1261.
[31] Y. Zhao, Z. Zhou, X. Liu, A. Ren, S. Ji, Y. Guan, Z. Liu, H. Liu, P. Li, F. Hu, Y. S. Zhao, *Adv. Opt. Mater.* **2023**, *11*, 2301239.
[32] H. Kim, W. Choi, Y. J. Kim, J. Kim, J. Ahn, I. Song, M. Kwak, J. Kim, J. Park, D. Yoo, J. Park, S. K. Kwak, J. H. Oh, *Sci. Adv.* **2024**, *10*, eado5942.
[33] A. Ishii, T. Miyasaka, *Sci. Adv.* **2020**, *6*, eabd3274
[34] S. Liu, F. Yu, X. Liu, H. Zhang, M. Ma, S. Zhang, H. Guo, H. Hu, C. Yuan, Z. Zheng, Y. Wu, W.-H. Zhu, *Newton* **2025**, *1*, 100003.
[35] M. Kepenekian, J. Even, *J. Phys. Chem. Lett.* **2017**, *8*, 3362.
[36] D. Niesner, M. Wilhelm, I. Levchuk, A. Osvet, S. Shrestha, M. Batentschuk, C. Brabec, T. Fauster, *Phys. Rev. Lett.* **2016**, *117*, 126401.
[37] Q. Wei, Z. Ning, *ACS Mater. Lett.* **2021**, *3*, 1266.
[38] Y. Dong, M. P. Hautzinger, M. A. Haque, M. C. Beard, *Annu. Rev. Phys. Chem.* **2025**, *76*, 519.
[39] T. Feng, Z. Wang, Z. Zhang, J. Xue, H. Lu, *Nanoscale* **2021**, *13*, 18925.
[40] H. Lu, Z. V. Vardeny, M. C. Beard, *Nat. Rev. Chem.* **2022**, *6*, 470.
[41] Z. Li, E. Hong, X. Zhang, M. Deng, X. S. Fang, *J. Phys. Chem. Lett.* **2022**, *13*, 1215.
[42] Z. Li, T. Yan, X. S. Fang, *Nat. Rev. Mater.* **2023**, *8*, 587.
[43] Y. Hu, X. Zhang, X. Mo, J. Chu, X. S. Fang, Z. Li, *Adv. Funct. Mater.* **2025**, *35*, 2412015.
[44] R. Naaman, Y. Paltiel, D. H. Waldeck, *Nat. Rev. Chem.* **2019**, *3*, 250.
[45] D. G. Billing, A. Lemmerer, *Acta Cryst.* **2003**, *59*, m381.
[46] D. G. Billing, A. Lemmerer, *CrystEngComm* **2006**, *8*, 686.
[47] J. Ahn, E. Lee, J. Tan, W. Yang, B. Kim, J. Moon, *Mater. Horiz.* **2017**, *4*, 851.
[48] J. Ma, C. Fang, C. Chen, L. Jin, J. Wang, S. Wang, J. Tang, D. Li, *ACS Nano* **2019**, *13*, 3659.
[49] J. Bai, H. Wang, J. Ma, Y. Zhao, H. Lu, Y. Zhang, S. Gull, T. Qiao, W. Qin, Y. Chen, L. Jiang, G. Long, Y. Wu, *J. Am. Chem. Soc.* **2024**, *146*, 18771.
[50] H. Kim, R. M. Kim, S. D. Namgung, N. H. Cho, J. B. Son, K. Bang, M. Choi, S. K. Kim, K. T. Nam, J. W. Lee, J. H. Oh, *Adv. Sci.* **2022**, *9*, 2104598.
[51] Q. Liu, Q. Wei, H. Ren, L. Zhou, Y. Zhou, P. Wang, C. Wang, J. Yin, M. Li, *Nat. Commun.* **2023**, *14*, 7179.
[52] G. Chen, X. Liu, J. An, S. Wang, X. Zhao, Z. Gu, C. Yuan, X. Xu, J. Bao, H.-S. Hu, J. Li, X. Wang, *Nat. Chem.* **2023**, *15*, 1581.
[53] X. Shang, L. Wan, L. Wang, F. Gao, H. Li, *J. Mater. Chem. C* **2022**, *10*, 2400.
[54] H. Wang, J. Li, H. Lu, S. Gull, T. Shao, Y. Zhang, T. He, Y. Chen, T. He, G. Long, *Angew. Chem., Int. Ed.* **2023**, *62*, 202309600.
[55] H. Peng, Y. Qin, X. G. Chen, X. J. Song, R. G. Xiong, W. Q. Liao, *Angew. Chem., Int. Ed.* **2025**, *64*, 202500285.
[56] T. Duan, Y. Zhou, *Adv. Energy Mater.* **2023**, *13*, 2200792.
[57] D. Fu, J. Xin, Y. He, S. Wu, X. Zhang, X. M. Zhang, J. Luo, *Angew. Chem., Int. Ed.* **2021**, *60*, 20021.
[58] Y. Fu, H. Zhu, J. Chen, M. P. Hautzinger, X. Y. Zhu, S. Jin, *Nat. Rev. Mater.* **2019**, *4*, 169.
[59] L. N. Quan, J. Kang, C.-Z. Ning, P. Yang, *Chem. Rev.* **2019**, *119*, 9153.
[60] L. Fang, H. Luo, X. Cao, S. Zheng, X. Cai, J. Wang, *Optica* **2019**, *6*, 61.
[61] Z. Zhang, Z. Wang, H. H. Y. Sung, I. D. Williams, Z.-G. Yu, H. Lu, *J. Am. Chem. Soc.* **2022**, *144*, 22242.
[62] U. Makhija, P. K. Rajput, P. Parthiban, A. Nag, *J. Chem. Phys.* **2024**, *160*, 021102.
[63] A. Salij, R. H. Goldsmith, R. Tempelaar, *J. Am. Chem. Soc.* **2021**, *143*, 21519.
[64] G. Albano, G. Pescitelli, L. Di Bari, *Chem. Rev.* **2020**, *120*, 10145.
[65] T. Dutta, D. Swain, A. Nag, *Angew. Chem., Int. Ed.* **2025**, *64*, 202422550.
[66] R. Naaman, D. H. Waldeck, *J. Phys. Chem. Lett.* **2012**, *3*, 2178.
[67] M. Kettner, B. Göhler, H. Zacharias, D. Mishra, V. Kiran, R. Naaman, C. Fontanesi, D. H. Waldeck, S. Sęk, J. Pawłowski, J. Juhaniewicz, *J. Phys. Chem. C* **2015**, *119*, 14542.
[68] F. Evers, A. Aharony, N. Bar-Gill, O. Entin-Wohlman, P. Hedegård, O. Hod, P. Jelinek, G. Kamieniarz, M. Lemeshko, K. Michaeli, V. Mujica, R. Naaman, Y. Paltiel, S. Refaely-Abramson, O. Tal, J. Thijssen, M. Thoss, J. M. van Ruitenbeek, L. Venkataraman, D. H. Waldeck, B. Yan, L. Kronik, *Adv. Mater.* **2022**, *34*, 2106629.
[69] R. Hu, W. Qin, *Laser Photonics Rev.* **2024**, *19*, 2400761.
[70] B. P. Bloom, Y. Paltiel, R. Naaman, D. H. Waldeck, *Chem. Rev.* **2024**, *124*, 1950.
[71] R. Naaman, D. H. Waldeck, *Annu. Rev. Phys. Chem.* **2015**, *66*, 263.
[72] A. Maiti, A. J. Pal, *Angew. Chem., Int. Ed.* **2022**, *134*, 202214161.
[73] A. Pietropaolo, A. Mattoni, G. Pica, M. Fortino, G. Schifino, G. Grancini, *Chem* **2022**, *8*, 1231.
[74] J. Wang, H. Lu, X. Pan, J. Xu, H. Liu, X. Liu, D. R. Khanal, M. F. Toney, M. C. Beard, Z. V. Vardeny, *ACS Nano* **2021**, *15*, 588.
[75] R. Pan, X. Tang, L. Kan, Y. Li, H. Yu, K. Wang, *Nanoscale* **2023**, *15*, 3300.
[76] Y. H. Kim, R. Song, J. Hao, Y. Zhai, L. Yan, T. Moot, A. F. Palmstrom, R. Brunecky, W. You, J. J. Berry, J. L. Blackburn, M. C. Beard, V. Blum, J. M. Luther, *Adv. Funct. Mater.* **2022**, *32*, 2200454.
[77] Z.-G. Yu, *J. Phys. Chem. Lett.* **2020**, *11*, 8638.
[78] S.-H. Yang, R. Naaman, Y. Paltiel, S. S. P. Parkin, *Nat. Rev. Phys.* **2021**, *3*, 328.
[79] M. K. Jana, R. Song, H. Liu, D. R. Khanal, S. M. Janke, R. Zhao, C. Liu, Z. Valy Vardeny, V. Blum, D. B. Mitzi, *Nat. Commun.* **2020**, *11*, 4699.
[80] J. Zhao, H. Huo, Y. Zhao, Y. Guo, M. Dong, Y. Fu, J. Zhang, Z. Gao, L. Kang, *Chem. Mater.* **2023**, *35*, 4347.
[81] S. Chakraborty, M. K. Nazeeruddin, *J. Phys. Chem. Lett.* **2021**, *12*, 361.
[82] S. A. Wolf, D. D. Awschalom, R. A. Buhrman, J. M. Daughton, S. von Molnár, M. L. Roukes, A. Y. Chtchelkanova, D. M. Treger, *Science* **2001**, *294*, 1488.
[83] B. Maurer, C. Vorwerk, C. Draxl, *Phys. Rev. B* **2022**, *105*, 155149.
[84] Z. Ding, Q. Chen, Y. Jiang, M. Yuan, *JACS Au* **2024**, *4*, 1263.
[85] M. Kepenekian, R. Robles, C. Katan, D. Sapori, L. Pedesseau, J. Even, *ACS Nano* **2015**, *9*, 11557.
[86] Z. Guo, J. Li, R. Chen, T. He, *Prog. Quantum Electron.* **2022**, *82*, 100375.
[87] P. J. Huang, K. Taniguchi, M. Shigefuji, T. Kobayashi, M. Matsubara, T. Sasagawa, H. Sato, H. Miyasaka, *Adv. Mater.* **2021**, *33*, 2008611.
[88] P.-J. Huang, K. Taniguchi, H. Miyasaka, *J. Am. Chem. Soc.* **2019**, *141*, 14520.
[89] X. Liu, F. Zhang, P. Long, T. Lu, H. Zeng, Y. Liu, R. L. Withers, Y. Li, Z. Yi, *Adv. Mater.* **2018**, *30*, 1801619.
[90] M. Alexe, D. Hesse, *Nat. Commun.* **2011**, *2*, 256.
[91] Q. Guan, P. Xu, B. Xu, H. Ye, Z. K. Zhu, S. Wang, C. Zhang, H. Li, C. Ji, Z. Lin, J. Luo, *Adv. Sci.* **2024**, *12*, 2412506.
[92] T. Choi, S. Lee, Y. J. Choi, V. Kiryukhin, S.-W. Cheong, *Science* **2009**, *324*, 63.
[93] T. Zhu, J. Bie, C. Ji, X. Zhang, L. Li, X. Liu, X.-Y. Huang, W. Fa, S. Chen, J. Luo, *Nat. Commun.* **2022**, *13*, 7702.
[94] Z. K. Zhu, T. Zhu, S. You, P. Yu, J. Wu, Y. Zeng, Q. Guan, Z. Li, C. Qu, H. Zhong, L. Li, J. Luo, *Small* **2024**, *20*, 2307454.
[95] W. Guo, H. Xu, F. Sun, Y. Liu, Y. Ma, W. Liu, Y. Zhao, Z. Sun, J. Luo, *Angew. Chem., Int. Ed.* **2025**, *64*, 202421463.

[96] W. Wu, L. Li, D. Li, Y. Yao, Z. Xu, X. Liu, M. Hong, J. Luo, *Adv. Opt. Mater.* **2022**, *10*, 2102678.
[97] C. Zhang, Z. Wu, W. Zhang, Q. Guan, H. Ye, R. Li, H. Li, Z.-K. Zhu, P. Wang, Y. Wang, Y. Fang, J. Luo, *J. Am. Chem. Soc.* **2025**, *147*, 9686.
[98] T. Zhu, H. Wu, C. Ji, X. Zhang, Y. Peng, Y. Yao, H. Ye, W. Weng, W. Lin, J. Luo, *Adv. Opt. Mater.* **2022**, *10*, 2200146.
[99] Z. Li, C. Ji, Y. Fan, T. Zhu, S. You, J. Wu, R. Li, Z.-K. Zhu, P. Yu, X. Kuang, J. Luo, *J. Am. Chem. Soc.* **2023**, *145*, 25134.
[100] L. Guo, X. Liu, L. Gao, X. Wang, L. Zhao, W. Zhang, S. Wang, C. Pan, Z. Yang, *ACS Nano* **2022**, *16*, 1280.
[101] S. Li, X. Liu, H. Yang, H. Zhu, X. S. Fang, *Nat. Electron.* **2024**, *7*, 216.
[102] M. Deng, Z. Li, S. Liu, X. S. Fang, L. Wu, *Nat. Commun.* **2024**, *15*, 8789.
[103] Y. Dang, X. Liu, B. Cao, X. Tao, *Matter* **2021**, *4*, 794.
[104] W. Li, Z. Wang, F. Deschler, S. Gao, R. H. Friend, A. K. Cheetham, *Nat. Rev. Mater.* **2017**, *2*, 16099.
[105] J. Kang, J. H. Cho, *Phys. Chem. Chem. Phys.* **2020**, *22*, 13347.
[106] C. Zhou, Y. Chu, L. Ma, Y. Zhong, C. Wang, Y. Liu, H. Zhang, B. Wang, X. Feng, X. Yu, X. Zhang, Y. Sun, X. Li, G. Zhao, *Phys. Chem. Chem. Phys.* **2020**, *22*, 17299.
[107] Y. Shi, P. Duan, S. Huo, Y. Li, M. Liu, *Adv. Mater.* **2018**, *30*, 1705011.
[108] A. Forde, D. Ghosh, D. Kilin, A. C. Evans, S. Tretiak, A. J. Neukirch, *J. Phys. Chem. Lett.* **2022**, *13*, 686.
[109] X. Jin, M. Zhou, J. Han, B. Li, T. Zhang, S. Jiang, P. Duan, *Nano Res.* **2022**, *15*, 1047.
[110] M. Li, F. Fang, X. Huang, G. Liu, Z. Lai, Z. Chen, J. Hong, Y. Chen, R.-j. Wei, G.-H. Ning, K. Leng, Y. Shi, B. Tian, *Chem. Mater.* **2022**, *34*, 2955.
[111] X. Zhang, W. Weng, L. Li, H. Wu, Y. Yao, Z. Wang, X. Liu, W. Lin, J. Luo, *Small* **2021**, *17*, 2102884.
[112] X. Zhang, H. Ye, L. Liang, X. Niu, J. Wu, J. Luo, *ACS Appl. Mater. Interfaces* **2022**, *14*, 36781.
[113] M.-E. Sun, Y. Wang, F. Wang, J. Feng, L. Wang, H. Gao, G. Chen, J. Gu, Y. Fu, K. Bu, T. Fu, J. Li, X. Lü, L. Jiang, Y. Wu, S.-Q. Zang, *J. Am. Chem. Soc.* **2023**, *145*, 8908.
[114] L.-S. Li, Y.-H. Tan, W.-J. Wei, H.-Q. Gao, Y.-Z. Tang, X.-B. Han, *ACS Appl. Mater. Interfaces* **2021**, *13*, 2044.
[115] J.-M. Zhang, X.-B. Han, W. Wang, M.-L. Jin, C.-Q. Jing, C.-Y. Chai, C.-D. Liu, W. Zhang, *J. Mater. Chem. C* **2024**, *12*, 10200.
[116] X. Wang, Y. Wu, F. Gao, Y. Wang, *New J. Chem.* **2024**, *48*, 3192.
[117] S. Yang, G. Jang, C. U. Lee, J. Son, J. Lee, W. Jeong, D. G. Roe, J. H. Cho, J. Moon, *Adv. Funct. Mater.* **2024**, *34*, 2310917.
[118] B. Sun, X.-F. Liu, X.-Y. Li, Y. Zhang, X. Shao, D. Yang, H.-L. Zhang, *Chem. Mater.* **2020**, *32*, 8914.
[119] Q. A. Akkerman, L. Manna, *ACS Energy Lett.* **2020**, *5*, 604.
[120] L. Yao, G. Niu, J. Li, L. Gao, X. Luo, B. Xia, Y. Liu, P. Du, D. Li, C. Chen, Y. Zheng, Z. Xiao, J. Tang, *J. Phys. Chem. Lett.* **2020**, *11*, 1255.
[121] T. H. Moon, S.-J. Oh, K. M. Ok, *ACS Omega* **2018**, *3*, 17895.
[122] C. Li, Y. Wei, Y. Li, Z. Luo, Y. Liu, M. He, Y. Zhang, X. He, X. Chang, Z. Quan, *Small* **2024**, *20*, 2400338.
[123] T. Liu, W. Shi, W. Tang, Z. Liu, B. C. Schroeder, O. Fenwick, M. J. Fuchter, *ACS Nano* **2022**, *16*, 2682.
[124] X. Zhang, Z. Li, E. Hong, T. Yan, X. S. Fang, *Adv. Mater.* **2025**, *37*, 2412014.
[125] G. Long, C. Jiang, R. Sabatini, Z. Yang, M. Wei, L. N. Quan, Q. Liang, A. Rasmita, M. Askerka, G. Walters, X. Gong, J. Xing, X. Wen, R. Quintero-Bermudez, H. Yuan, G. Xing, X. R. Wang, D. Song, O. Voznyy, M. Zhang, S. Hoogland, W. Gao, Q. Xiong, E. H. Sargent, *Nat. Photonics* **2018**, *12*, 528.
[126] J. Ma, H. Wang, D. Li, *Adv. Mater.* **2021**, *33*, 2008785.
[127] D. Li, X. Liu, W. Wu, Y. Peng, S. Zhao, L. Li, M. Hong, J. Luo, *Angew. Chem., Int. Ed.* **2021**, *60*, 8415.
[128] J. Wang, C. Fang, J. Ma, S. Wang, L. Jin, W. Li, D. Li, *ACS Nano* **2019**, *13*, 9473.
[129] L. Tao, W. Tang, M. Yan, L. Ding, J. Wei, L. Wang, L. Li, L. Li, D. Yang, Y. Fang, *J. Mater. Chem. C* **2023**, *11*, 12392.
[130] C. U. Lee, S. Ma, J. Ahn, J. Kyhm, J. Tan, H. Lee, G. Jang, Y. S. Park, J. Yun, J. Lee, J. Son, J.-S. Park, J. Moon, *J. Am. Chem. Soc.* **2022**, *144*, 16020.
[131] H. Lee, S. Ma, S. Oh, J. Tan, C. U. Lee, J. Son, Y. S. Park, J. Yun, G. Jang, J. Moon, *Small* **2023**, *19*, 2304166.
[132] K. L. Svane, A. C. Forse, C. P. Grey, G. Kieslich, A. K. Cheetham, A. Walsh, K. T. Butler, *J. Phys. Chem. Lett.* **2017**, *8*, 6154.
[133] J. Son, S. Ma, Y.-K. Jung, J. Tan, G. Jang, H. Lee, C. U. Lee, J. Lee, S. Moon, W. Jeong, A. Walsh, J. Moon, *Nat. Commun.* **2023**, *14*, 3124.
[134] K.-z. Du, Q. Tu, X. Zhang, Q. Han, J. Liu, S. Zauscher, D. B. Mitzi, *Inorg. Chem.* **2017**, *56*, 9291.
[135] J. T. Lin, D. G. Chen, L. S. Yang, T. C. Lin, Y. H. Liu, Y. C. Chao, P. T. Chou, C. W. Chiu, *Angew. Chem., Int. Ed.* **2021**, *60*, 21434.
[136] J. Hu, I. W. H. Oswald, S. J. Stuard, M. M. Nahid, N. Zhou, O. F. Williams, Z. Guo, L. Yan, H. Hu, Z. Chen, X. Xiao, Y. Lin, Z. Yang, J. Huang, A. M. Moran, H. Ade, J. R. Neilson, W. You, *Nat. Commun.* **2019**, *10*, 1276.
[137] J. Son, G. Jang, S. Ma, H. Lee, C. U. Lee, S. Yang, J. Lee, S. Moon, W. Jeong, J. H. Park, J. Kim, D. H. Kim, J. S. Park, J. Moon, *Adv. Funct. Mater.* **2024**, *35*, 2413041.
[138] X. Fu, M. Wang, Y. Jiang, X. Guo, X. Zhao, C. Sun, L. Zhang, K. Wei, H.-Y. Hsu, M. Yuan, *Nano Lett.* **2023**, *23*, 6465.
[139] W. Choi, M. Kwak, J. Park, H. Kim, J. Kim, Y. Seo, D. Yoo, J. H. Oh, *Chem. Eng. J.* **2024**, *498*, 155504.
[140] Y. Xie, J. Morgenstein, B. G. Bobay, R. Song, N. A. M. S. Caturello, P. C. Sercel, V. Blum, D. B. Mitzi, *J. Am. Chem. Soc.* **2023**, *145*, 17831.
[141] L. Yan, M. K. Jana, P. C. Sercel, D. B. Mitzi, W. You, *J. Am. Chem. Soc.* **2021**, *143*, 18114.
[142] Z. K. Zhu, T. Zhu, S. You, P. Yu, J. Wu, Y. Zeng, Y. Jiang, X. Liu, L. Li, C. Ji, J. Luo, *Adv. Sci.* **2024**, *11*, 2307593.
[143] J. E. Spanier, V. M. Fridkin, A. M. Rappe, A. R. Akbashev, A. Polemi, Y. Qi, Z. Gu, S. M. Young, C. J. Hawley, D. Imbrenda, G. Xiao, A. L. Bennett-Jackson, C. L. Johnson, *Nat. Photonics* **2016**, *10*, 611.
[144] S. Ghosh, B. Pradhan, Y. Zhang, D. Rana, D. Naumenko, H. Amenitsch, J. Hofkens, A. Materny, *J. Phys. Chem. C* **2021**, *125*, 7799.
[145] R. Lu, Z. Wen, M. Zhao, J. Li, L. Zhang, Y. Yang, H. Jin, Y. Chen, S. Wang, S. Pan, *Adv. Opt. Mater.* **2023**, *11*, 2202290.
[146] X. Zhang, Y. Xu, A. N. Alphenaar, S. Ramakrishnan, Y. Zhang, A. J. Babatunde, Q. Yu, *ACS Nano* **2024**, *18*, 14605.
[147] T. Zhu, W. Weng, C. Ji, X. Zhang, H. Ye, Y. Yao, X. Li, J. Li, W. Lin, J. Luo, *J. Am. Chem. Soc.* **2022**, *144*, 18062.
[148] S. You, P. Yu, T. Zhu, Q. Guan, J. Wu, H. Dai, H. Zhong, Z.-K. Zhu, J. Luo, *Mater. Horiz.* **2023**, *10*, 5307.
[149] T. L. Leung, I. Ahmad, A. A. Syed, A. M. C. Ng, J. Popović, A. B. Djurišić, *Commun. Mater.* **2022**, *3*, 63.
[150] H. Song, M. Kwak, W. Choi, D. Yoo, J. H. Oh, *Adv. Opt. Mater.* **2024**, *12*, 2401427.
[151] W. Chen, Y. Shi, J. Chen, P. Ma, Z. Fang, D. Ye, Y. Lu, Y. Yuan, J. Zhao, Z. Xiao, *Adv. Mater.* **2021**, *33*, 2104842.
[152] Y. Zhao, X. Yin, Z. Gu, M. Yuan, J. Ma, T. Li, L. Jiang, Y. Wu, Y. Song, *Adv. Funct. Mater.* **2023**, *33*, 2306199.
[153] S. Ma, Y.-K. Jung, J. Ahn, J. Kyhm, J. Tan, H. Lee, G. Jang, C. U. Lee, A. Walsh, J. Moon, *Nat. Commun.* **2022**, *13*, 3259.
[154] A. Privitera, M. Righetto, F. Cacialli, M. K. Riede, *Adv. Opt. Mater.* **2021**, *9*, 2100215.
[155] H. Lu, C. Xiao, R. Song, T. Li, A. E. Maughan, A. Levin, R. Brunecky, J. J. Berry, D. B. Mitzi, V. Blum, M. C. Beard, *J. Am. Chem. Soc.* **2020**, *142*, 13030.
[156] C. Li, Z. Song, C. Chen, C. Xiao, B. Subedi, S. P. Harvey, N. Shrestha, K. K. Subedi, L. Chen, D. Liu, Y. Li, Y.-W. Kim, C.-S. Jiang, M. J. Heben, D. Zhao, R. J. Ellingson, N. J. Podraza, M. Al-Jassim, Y. Yan, *Nat. Energy* **2020**, *5*, 768.

[157] J. Hu, X. Wen, D. Yang, Y. Chen, Z. Liu, D. Li, *Nano Lett.* **2024**, *24*, 1001.
[158] T. Zhu, X. Li, P. Yu, Z. Zhu, M. Li, R. Li, S. Han, H. Ye, C. Ji, J. Luo, *Chem* **2024**, *10*, 882.
[159] K. Kim, Y. Li, K. M. Ok, *J. Am. Chem. Soc.* **2025**, *147*, 2880.
[160] X. Niu, Y. Li, H. Lu, Z. Wang, Y. Zhang, T. Shao, H. Wang, S. Gull, B. Sun, H.-L. Zhang, Y. Chen, K. Wang, Y. Du, G. Long, *Nat. Commun.* **2025**, *16*, 2525.
[161] J. Ahn, S. Ma, J.-Y. Kim, J. Kyhm, W. Yang, J. A. Lim, N. A. Kotov, J. Moon, *J. Am. Chem. Soc.* **2020**, *142*, 4206.
[162] S. Driessen, S. Sarigul-Ozbek, C. M. Sutter-Fella, S. Tao, *J. Phys. Energy* **2024**, *6*, 042001.
[163] C. Chen, Z. Zhang, C. Wang, T. Geng, Y. Feng, J. Ding, Q. Ma, W. Gao, M. Li, J. Chen, J. x. Tang, *Small* **2024**, *20*, 2311377.
[164] H. Wang, L. Yao, Y. Zhan, H. Yu, S. Wu, X. Liu, *ACS Appl. Mater. Interfaces* **2025**, *17*, 3716.
[165] X.-K. Liu, W. Xu, S. Bai, Y. Jin, J. Wang, R. H. Friend, F. Gao, *Nat. Mater.* **2021**, *20*, 10.
[166] L. Tao, H. Zhan, Y. Cheng, C. Qin, L. Wang, *J. Phys. Chem. Lett.* **2023**, *14*, 2317.
[167] J. Lu, Y. Xue, K. Bernardino, N.-N. Zhang, W. R. Gomes, N. S. Ramesar, S. Liu, Z. Hu, T. Sun, A. F. d. Moura, N. A. Kotov, K. Liu, *Science* **2021**, *371*, 1368.
[168] C.-S. Ho, A. Garcia-Etxarri, Y. Zhao, J. Dionne, *ACS Photonics* **2017**, *4*, 197.
[169] X. Lü, Y. Wang, C. C. Stoumpos, Q. Hu, X. Guo, H. Chen, L. Yang, J. S. Smith, W. Yang, Y. Zhao, H. Xu, M. G. Kanatzidis, Q. Jia, *Adv. Mater.* **2016**, *28*, 8663.
[170] A. Jaffe, Y. Lin, W. L. Mao, H. I. Karunadasa, *J. Am. Chem. Soc.* **2017**, *139*, 4330.
[171] Y. Zhang, M. Sun, N. Zhou, B. Huang, H. Zhou, *J. Phys. Chem. Lett.* **2020**, *11*, 7610.
[172] Y.-H. Kim, Y. Zhai, E. A. Gaulding, S. N. Habisreutinger, T. Moot, B. A. Rosales, H. Lu, A. Hazarika, R. Brunecky, L. M. Wheeler, J. J. Berry, M. C. Beard, J. M. Luther, *ACS Nano* **2020**, *14*, 8816.
[173] M. A. Haque, A. Grieder, S. P. Harvey, R. Brunecky, J. Y. Ye, B. Addison, J. Zhang, Y. Dong, Y. Xie, M. P. Hautzinger, H. H. Walpitage, K. Zhu, J. L. Blackburn, Z. V. Vardeny, D. B. Mitzi, J. J. Berry, S. R. Marder, Y. Ping, M. C. Beard, J. M. Luther, *Nat. Chem.* **2025**, *17*, 29.
[174] Z. N. Georgieva, B. P. Bloom, S. Ghosh, D. H. Waldeck, *Adv. Mater.* **2018**, *30*, 1800097.
[175] Q. Cao, R. Song, C. C. S. Chan, Z. Wang, P. Y. Wong, K. S. Wong, V. Blum, H. Lu, *Adv. Opt. Mater.* **2023**, *11*, 2203125.
[176] L.-L. Xu, H.-F. Zhang, M. Li, S. W. Ng, J.-H. Feng, J.-G. Mao, D. Li, *J. Am. Chem. Soc.* **2018**, *140*, 11569.
[177] Y. Zhao, Y. Qiu, J. Feng, J. Zhao, G. Chen, H. Gao, Y. Zhao, L. Jiang, Y. Wu, *J. Am. Chem. Soc.* **2021**, *143*, 8437.
[178] Y. Zhao, X. Li, J. Feng, J. Zhao, Y. Guo, M. Yuan, G. Chen, H. Gao, L. Jiang, Y. Wu, *Giant* **2022**, *9*, 100086.
[179] M. Yuan, Y. Qiu, Y. Zhao, Y. Zhao, H. Li, X. Wei, G. Chen, J. Feng, H. Gao, J. Zhao, J. Zhao, L. Jiang, Y. Wu, *Sci. China Chem.* **2023**, *66*, 3602.
[180] Q. Liu, P. Wang, Q. Wei, L. Zhou, H. Ren, C. Wang, J. Peng, L. Zhao, M. Li, *Adv. Funct. Mater.* **2025**, *35*, 2415551.
[181] Z. Liu, C. Zhang, X. Liu, A. Ren, Z. Zhou, C. Qiao, Y. Guan, Y. Fan, F. Hu, Y. S. Zhao, *Adv. Sci.* **2021**, *8*, 2102065.
[182] Y. Zhao, M. Dong, J. Feng, J. Zhao, Y. Guo, Y. Fu, H. Gao, J. Yang, L. Jiang, Y. Wu, *Adv. Opt. Mater.* **2022**, *10*, 2102227.
[183] E. Radicchi, E. Mosconi, F. Elisei, F. Nunzi, F. De Angelis, *ACS Appl. Energy Mater.* **2019**, *2*, 3400.
[184] J.-W. Lee, Z. Dai, C. Lee, H. M. Lee, T.-H. Han, N. De Marco, O. Lin, C. S. Choi, B. Dunn, J. Koh, D. Di Carlo, J. H. Ko, H. D. Maynard, Y. Yang, *J. Am. Chem. Soc.* **2018**, *140*, 6317.
[185] H. Zhu, Q. Wang, K. Sun, W. Chen, J. Tang, J. Hao, Z. Wang, J. Sun, W. C. H. Choy, P. Müller-Buschbaum, X. W. Sun, D. Wu, K. Wang, *ACS Appl. Mater. Interfaces* **2023**, *15*, 9978.
[186] L. Scalon, J. Brunner, M. G. D. Guaita, R. Szostak, M. Albaladejo-Siguan, T. Kodalle, L. A. Guerrero-León, C. M. Sutter-Fella, C. C. Oliveira, Y. Vaynzof, A. F. Nogueira, *Adv. Opt. Mater.* **2024**, *12*, 2300776.
[187] L. Chen, F. Tavormina, L. D. Mario, M. Pitaro, G. Portale, N. Masciocchi, A. Guagliardi, M. A. Loi, *Adv. Energy Mater.* **2025**, https://doi.org/10.1002/aenm.202405941.
[188] M. I. Saidaminov, I. Spanopoulos, J. Abed, W. Ke, J. Wicks, M. G. Kanatzidis, E. H. Sargent, *ACS Energy Lett.* **2020**, *5*, 1153.
[189] S. Tian, G. Li, R. C. Turnell-Ritson, Z. Fei, A. Bornet, M. K. Nazeeruddin, P. J. Dyson, *Angew. Chem., Int. Ed.* **2024**, *63*, 202407193.
[190] D. Di Girolamo, J. Pascual, M. H. Aldamasy, Z. Iqbal, G. Li, E. Radicchi, M. Li, S.-H. Turren-Cruz, G. Nasti, A. Dallmann, F. De Angelis, A. Abate, *ACS Energy Lett.* **2021**, *6*, 959.
[191] W. D. Rice, W. Liu, T. A. Baker, N. A. Sinitsyn, V. I. Klimov, S. A. Crooker, *Nat. Nanotechnol.* **2016**, *11*, 137.
[192] P. Zhao, B. J. Kim, X. Ren, D. G. Lee, G. J. Bang, J. B. Jeon, W. B. Kim, H. S. Jung, *Adv. Mater.* **2018**, *30*, 1802763.
[193] S. L. Gibbs, C. Dean, J. Saad, B. Tandon, C. M. Staller, A. Agrawal, D. J. Milliron, *Nano Lett.* **2020**, *20*, 7498.
[194] C. Zhang, Z. S. Li, X. Y. Dong, Y. Y. Niu, S. Q. Zang, *Adv. Mater.* **2022**, *34*, 2109496.
[195] W. Zhang, H. Jiang, Y. Liu, Y. Hu, A. S. Palakkal, Y. Zhou, M. Sun, E. Du, W. Gong, Q. Zhang, J. Jiang, J. Dong, Y. Liu, D. Li, Y. Zhu, Y. Cui, X. Duan, *Nature* **2025**, *638*, 418.
[196] A. Cacciuto, S. Auer, D. Frenkel, *Nature* **2004**, *428*, 404.
[197] L. Martiradonna, *Nat. Mater.* **2018**, *17*, 377.
[198] O. Volochanskyi, G. Haider, E. A. Alharbi, G. Kakavelakis, M. Mergl, M. K. Thakur, A. Krishna, M. Graetzel, M. Kalbáč, *ACS Appl. Mater. Interfaces* **2024**, *16*, 52789.
[199] Y. Liu, Y. Jiang, Z. Xu, L. Li, D. Zhang, W. Zheng, D. Liang, B. Zheng, H. Liu, X. Sun, C. Zhu, L. Lin, X. Zhu, H. Duan, Q. Yuan, X. Wang, S. Wang, D. Li, A. Pan, *Adv. Opt. Mater.* **2022**, *10*, 2200183.
[200] Z. Zhang, W. Liang, J. Xue, X. Li, K. Wu, H. Lu, *ACS Nano* **2024**, *18*, 35088.
[201] Z. Zeng, H. Lu, Z. Yang, H. Wu, C. Zhang, G. Long, Y. Du, *Adv. Phys. Res.* **2024**, *3*, 2400064.
[202] I. Song, J. Ahn, H. Ahn, S. H. Lee, J. Mei, N. A. Kotov, J. H. Oh, *Nature* **2023**, *617*, 92.
[203] S. Hu, B. Tang, S. V. Kershaw, N. A. Kotov, R. Andrey, *ACS Appl. Mater. Interfaces* **2024**, *16*, 12965.
[204] G. Long, G. Adamo, J. Tian, M. Klein, H. N. S. Krishnamoorthy, E. Feltri, H. Wang, C. Soci, *Nat. Commun.* **2022**, *13*, 1551.
[205] C.-Y. Li, C. Chen, Y. Liu, J. Su, D.-X. Qi, J. He, R.-H. Fan, Q. Cai, Q. Li, R. Peng, X.-R. Huang, M. Wang, *Opt. Lett.* **2022**, *47*, 565.
[206] S. Liu, X. Liu, Y. Wu, D. Zhang, Y. Wu, H. Tian, Z. Zheng, W.-H. Zhu, *Matter* **2022**, *5*, 2319.
[207] X. Zhang, L. Li, Y. Chen, C. Valenzuela, Y. Liu, Y. Yang, Y. Feng, L. Wang, W. Feng, *Angew. Chem., Int. Ed.* **2024**, *63*, 202404202.
[208] Y. Feng, G. Gao, X. Wen, Z. Chen, J. Huang, C. Yang, X. F. Jiang, L. Polavarapu, G. Zhou, X. Hu, *Adv. Funct. Mater.* **2025**, *35*, 2421338.
[209] Y. Gu, Z. Li, M. Deng, X. Zhang, Y. Hu, L. Su, X. S. Fang, *Laser Photonics Rev.* **2025**, https://doi.org/10.1002/lpor.202501468.
[210] Z. Guo, J. Li, R. Liu, Y. Yang, C. Wang, X. Zhu, T. He, *Nano Lett.* **2023**, *23*, 7434.
[211] J. Pittrich, K. Liang, L. Dörringer, R. Kienberger, U. Heiz, A. Kartouzian, H. Iglev, *Appl. Surf. Sci.* **2025**, *680*, 161331.
[212] D. Okada, *Chem. - Eur. J.* **2025**, *31*, 202404034.
[213] H. Lee, M. J. Huttunen, K. J. Hsu, M. Partanen, G. Y. Zhuo, M. Kauranen, S. W. Chu, *Biomed. Opt. Express* **2013**, *4*, 909.

[214] D. J. Kissick, D. Wanapun, G. J. Simpson, *Annu. Rev. Anal. Chem.* **2011**, *4*, 419.
[215] H. Kim, K. Lee, G. Zan, E. Shin, W. Kim, K. Zhao, G. Jang, J. Moon, C. Park, *ACS Nano* **2025**, *19*, 691.
[216] W. He, C. Chen, S. Wu, W. P. D. Wong, Z. Wu, K. Chang, J. Wang, H. Gao, K. P. Loh, *J. Am. Chem. Soc.* **2025**, *147*, 811.
[217] D. Wang, S. Wang, Y. Dong, X. Wu, J. Shen, S. Feng, Z. Wang, W. Huang, *Adv. Mater.* **2025**, *37*, 2419747.
[218] S. Dan, S. Paramanik, A. J. Pal, *ACS Nano* **2024**, *18*, 14457.
[219] R. F. Service, *Science* **2001**, *292*, 2412.
[220] N. Gisin, R. Thew, *Nat. Photonics* **2007**, *1*, 165.
[221] J. Xiao, H. Zheng, R. Wang, Y. Wang, S. Hou, *J. Mater. Chem. A* **2022**, *10*, 19367.